

ABSTRACT

Title of dissertation: A HIGHLY EFFICIENT, MEGAWATT CLASS
CONSTANT IMPEDANCE TUNABLE
POWER EXTRACTION CIRCUIT FOR
MOBILE IONOSPHERIC HEATERS

Amith Hulikal Narayan
Doctor of Philosophy, 2020

Dissertation directed by: Professor Thomas M Antonsen Jr
Department of Electrical Engineering

Ionospheric modification (IM) refers to changes in the ambient properties of the ionosphere that are produced by humans. The ability to control and exploit ionospheric processes helps us understand naturally occurring phenomena like aurora, scintillations, and airglow. It also helps us improve trans-ionospheric communication and develop new applications that take advantage of the ionosphere as an active plasma medium. Ionospheric Heaters broadcast high power radio waves, typically in the radio frequency (RF) band, to modify the ionosphere in a controlled manner. These facilities are permanent terrestrial installations and do not presently support study at different latitudes. However, past IM experiments conducted at high latitudes across the world indicate a strong dependence of ionospheric processes on the geomagnetic latitude.

Mobile Ionospheric Heaters will allow for the first time, quantitative exploration of the ionosphere at different geomagnetic latitudes. These mobile structures

must be relatively smaller than the existing arrays (small enough to fit on the barge of a ship) and highly efficient at the same time. The size and efficiency of the terrestrial heating units prevent their reuse in mobile structures. These factors motivate the need for developing novel heater units. Our research focused on a new high power, high-efficiency RF source that consists of a gridless tetrode RF tube and a highly efficient power extraction circuit. My research addresses the characterization and optimization of the power extraction circuit.

The power extraction circuit in the RF device under study converts the kinetic energy of a temporally modulated electron beam into electromagnetic energy. The beam is collected on an electrode surface and the resulting current is passed through the circuit. The circuit generates a potential in response to the current, and that potential is used to decelerate the beam. The circuit must be tunable to cover the desired broad frequency range (3 -10 MHz), and the decelerating voltage should be independent of frequency to maintain high efficiency.

In this relatively low frequency range lumped element circuits are considered instead of cavities given the size limitations imposed. To achieve high power a high voltage beam is required. Consequently, matching the relatively high electron beam impedance ($5 \text{ k}\Omega$) to the load antenna (50Ω) creates situations where high Q resonant circuits are necessary to achieve the high efficiencies required. We design a pi-circuit to achieve the impedance matching and validate the design experimentally.

Although experiments validate our design, measured efficiencies are too low because of parasitics in the circuit elements. The parasitics include the proximity effect and self-resonance in the elements. We model these effects that enhance the

losses and limit the efficiency of the circuit.

Our research finds that the impedance transformation from beam to load (two orders of magnitude) imposes severe restrictions on single-stage design. Additionally, measurements of high Q components aren't very reliable at higher frequencies. We propose a two-stage power extraction circuit that resolves both of these problems. Simulation results show a circuit design that is expected to yield the desired efficiency. The findings from the research in this thesis would help in the eventual construction and testing of the MW RF heating system that would facilitate a mobile heater for IM research in the future.

A HIGHLY EFFICIENT, MEGAWATT CLASS,
CONSTANT IMPEDANCE TUNABLE POWER EXTRACTION
CIRCUIT
FOR MOBILE IONOSPHERIC HEATERS

by

Amith Hulikal Narayan

Dissertation submitted to the Faculty of the Graduate School of the
University of Maryland, College Park in partial fulfillment
of the requirements for the degree of
Doctor of Philosophy
2020

Advisory Committee:

Professor Thomas M Antonsen Jr

Professor Edward Ott

Professor Neil Goldsman

Professor Adil Hassam (Dean's Representative)

Dr. Brian Beaudoin

Dr. Antonio Ting

Dr. Gregory Nusinovich

Dedication

I would like to dedicate this to my aunt, Usha Tirumalai Santhanam, my uncle, Chakrapani Hulikal Shamaiyengar, my brother, Thejas and my wife Mouna . Your unconditional love and support have made this work achievable.

Acknowledgments

I owe my gratitude to all the people who have made this thesis possible and because of whom my graduate experience has been one that I will cherish forever.

First and foremost I'd like to thank my advisor, Professor Thomas M Antonsen Jr for giving me an invaluable opportunity to work on interesting projects over the past six years. He has always made himself available for help and advice and there has never been an occasion when I've knocked on his door and he hasn't given me time. It has been a pleasure to work with and learn from such an extraordinary individual. I am eternally indebted to him for his robust support all along these years.

I would also like to thank my co-advisors, Dr. Brian Beaudoin and Dr. Antonio Ting. Without Brian's extraordinary help at the lab in the initial days, I would be lost for a long time. Thanks are due to Dr. Antonio Ting, for helping me with experiments and editing this thesis. His intuition and insights have helped me think quicker on my feet in a laboratory setup. I would also like to thank Dr. Gregory Nusinovich for being the gentle force of guidance through out these years. I thank Professor Edward Ott , Professor Goldsman and Professor Adil Hassam for agreeing to serve on my thesis committee and for sparing their invaluable time reviewing the manuscript.

My colleagues at the IREAP have enriched my graduate life in many ways and deserve a special mention. Charles Turner helped me start-off my simulations by designing the first transformer on ANSYS. Nikhil Goyal helped me learn Autodesk

design software. Dr. John Rodgers gave us the first idea of the pi circuit as a power extraction circuit. I would also like to acknowledge help and support from some of the staff members: Thanks to Nancy Boone and Dorothea Brosius for all their help with administrative work.

I owe my deepest thanks to my family - my aunt and uncle, my wife and my brother who have always stood by me and guided me through my career, and have pulled me through against impossible odds at times. Words cannot express the gratitude I owe them.

Thanks to Jayakrishnan, for being a fellow traveller on this journey.

I would like to acknowledge financial support from the Air Force Office of Scientific Research (AFOSR) for our research.

It is impossible to remember all, and I apologize to those I've inadvertently left out. Lastly, thank you all and thank God!

Contents

Dedication	ii
Acknowledgements	iii
List of Figures	vii
1 Introduction to Mobile Ionospheric Heaters	1
1.1 Motivation	1
1.2 History	3
1.2.1 Ionospheric Modification	5
1.2.2 Ionospheric Heaters	6
1.3 Mobile Ionospheric Heaters	8
1.3.1 RF Power Source	9
1.3.2 Power Extraction Circuit	11
1.4 Goal for the Research	14
2 Power Extraction Circuit for 70 kV-30 A Gun	15
2.1 Introduction	15
2.2 Design of a Single Stage π -Circuit	17
2.3 Simulations and Cold Test Experiments	23
2.4 Experiments on the NRL Gun	25
2.4.1 Results	30
2.5 Discussion and Conclusion	34
3 Inductor Design: A Novel Approach	39
3.1 Introduction	39
3.2 Inductor Parasitics	41
3.2.1 Skin Effect	43
3.2.2 Proximity Effect	46
3.2.3 Self Resonance	48
3.3 Modelling Proximity Effect in Inductors	49
3.4 Inductor Design for the 70 kV - 30 A Gun Configuration	55
3.5 Measurements on the Test Coils	58

4	Design of Two-Stage Power Extraction Circuit	61
4.1	Introduction	61
4.2	Two-Stage Power Extraction Circuit	62
4.2.1	Losses	66
4.2.2	Tunability	70
4.3	Simulations & Results	70
5	Conclusion	74
	Bibliography	78

List of Figures

1.1	Heater facility locations around the world.	7
1.2	Schematic view of the IOT and its circuitry.	10
1.3	Mod anode voltage (blue) and the Beam current (red) as function of time. When the mode anode voltage is positive compared to emitter, beam current is ON.	11
1.4	Circuit diagram of the pi-circuit used for the power extraction from the IOT.	12
2.1	Cavity resonators used in different facilities. (a) Cavities of different sizes. (b) 350 MHz, 4-cell, Nb on Cu. (c) 1300 MHz 9-cell (d) 1500 MHz, 5-cell. Picture Courtesy: Jean Delayen [19]	16
2.2	Circuit diagram of the π -circuit used for the power extraction from the gridless tetrode.	18
2.3	Plot of Power Ratio $v/s \omega L_{12}/(\alpha R_L)$ (blue line) . Plot of $\omega C_2 R_L v/s \omega L_{12}/(\alpha R_L)$ (red line)	21
2.4	Actual experimental π -circuit setup for the 70kV-30A cold test case.	24
2.5	Plots for Gap Impedance as a function of Frequency.	25
2.6	Power Extraction Circuit and the low power IOT electron gun at NRL. The inductor is made of copper tubing, and the capacitor of the π -circuit sits on top of the gridded gun.	27
2.7	Measured (blue) and simulated (red) V_{in} (a) and V_{out} (b) versus time from the π -circuit. For comparisons, V_{in} and V_{out} simulations are displaced by 1 kV and 0.1 kV, respectively.	31
2.8	$V_{in}(t)$ at a capacitance C_2 of 2.7 nF, an RF drive frequency of 4.09 MHz (blue), $I_{beam}(t)$ measured as a voltage across 50 Ω connected to the collector and with the π -circuit removed, a solenoid current of 1.8 A, and an RF drive frequency of 4.09 MHz (green).	32
2.9	Measured (blue) and simulated (red) V_{in} and V_{out} versus time from the π -circuit. For comparisons, V_{in} and V_{out} simulations are displaced by 1 kV and 0.1 kV, respectively.	33
2.10	Measured (blue) and simulated (red) V_{in} and V_{out} versus time from the π -circuit. For comparisons, V_{in} and V_{out} simulations are displaced by 1 kV and 0.1 kV, respectively.	34

2.11	$V_{in}(t)$ at a capacitance C_2 of 2.7 nF, an RF drive frequency of 3.1 MHz (blue), $I_{beam}(t)$ measured as a voltage across 50Ω connected to the collector and with the π -circuit removed, a solenoid current of 1.8 A, and an RF drive frequency of 3.1 MHz (green).	35
2.12	Measured (blue) and simulated (red) V_{in} and V_{out} versus time from the π -circuit. For comparisons, V_{in} and V_{out} simulations are displaced by 1 kV and 0.1 kV, respectively.	36
2.13	Measured Q versus capacitance C_2 at an RF drive frequency of 4.09 MHz	37
2.14	Measured Q versus capacitance C_2 at an RF drive frequency of 3.1 MHz	38
3.1	A π -circuit as a simple power extraction circuit.	41
3.2	A sample solenoidal inductor coil [31]	42
3.3	Semi-infinite conductor in a magnetic field.	44
3.4	Comparison between DC and AC current flow. On the left, DC current flow is uniform in a wire. On the right, the AC current accumulates towards the surface.	45
3.5	Proximity Effect: (a) current flowing in the same direction (b) current flowing in the opposite direction	47
3.6	A simple parasitic model of the inductor (left). Inductance (black) and impedance (blue) plot as a function of frequency for typical inductor (right). Above the SRF, the coil behaves as a capacitor	48
3.7	A 2D Ansys Maxwell simulation example to explain different variables and boundaries.	49
3.8	Conductors at the edge of solenoidal coil have non uniform current densities	50
3.9	Conductors at the centre of solenoidal coil have a relatively uniform current distribution	51
3.10	Resistance as a function of the Turn Number for an inductor coil of turns, $N = 101$, $SL = 24cm$, $SR = 8cm$, $WR = 0.9mm$, $Pitch = 2.4mm$, at a frequency, $f = 4MHz$	52
3.11	E as a function of $Pitch/WR$ for different skin depth ratios	53
3.12	E as a function of $Pitch/WR$ for different radii ratios (SR/WR)	53
3.13	E as a function of $Pitch/WR$ for different aspect ratios (SL/SR)	54
3.14	Measurement accuracy chart (Source: Keysight Technologies Impedance Analyzer Manual)	59
4.1	A two stage power extraction circuit design	63
4.2	Finding the Operating Point with losses minimized.	67
4.3	PSpice simulation schematic for the two stage power extraction circuit.	71
4.4	V_{RF} (blue) and V_L (red) plots as a function of the frequency in two stage circuit.	72
4.5	R_{gap} (blue) and X_{gap} (red) plots as a function of the frequency in two stage circuit.	73

Chapter 1: Introduction to Mobile Ionospheric Heaters

1.1 Motivation

The ionosphere is the ionized part of earth's upper atmosphere, from about 60 km (37 mi) to 1,000 km (620 mi) altitude. It is ionized by ultraviolet, X-ray and shorter wavelengths of the incoming solar radiation. These radiations contain sufficient energy to dislodge an electron from a neutral gas atom upon absorption. The degree of ionization depends upon the intensity of incoming radiation, and on the chemical follow-up reactions which tend to restore electrical neutrality. As the air is so thin at these altitudes, free electrons can exist for short periods of time before recombination. The ionosphere, is thus a good example for naturally occurring plasma.

Ionospheric modification refers to changes in the ambient properties of the ionosphere that are produced by humans. This ability to control and exploit triggered ionospheric processes help us understand phenomena like *aurora*, *scintillations*, and *airglow* [1- 2]. While naturally occurring events can have pronounced and long-lasting effect on the ionosphere, we are concerned with effects that are repeatable and controllable. It also helps us improve trans-ionospheric communication and develop new applications that take advantage of the ionosphere as an

active plasma medium.

Ionospheric Heaters broadcast high power radio waves typically in the RF band to modify the ionosphere in a controlled manner. These heaters have successfully reproduced several types of naturally occurring phenomena like *airglow*, *scintillation* and *electron density channels and layers*[3]. High Frequency Active Auroral Research Program (HAARP) in Alaska, European Incoherent Scatter Scientific Association (EISCAT) in Norway are some of the heating facilities around the world. These facilities are permanent terrestrial installations and do not presently support study at different latitudes. However, past IM experiments conducted at high latitudes across the world indicate a strong dependence of ionospheric processes on the geomagnetic latitude [4].

Mobile Ionospheric Heaters will allow for the first time, quantitative exploration of the ionosphere at different geomagnetic latitudes. They have three significant sub-systems: an RF Power Source, a Power Extraction Circuit, and an Antenna. These mobile structures must be relatively smaller (small enough to fit on the barge of a ship) and highly efficient at the same time. The size and efficiency of the terrestrial heating units prevent their reuse in mobile structures. These factors motivate the need for developing a novel, efficient, mobile high power Ionospheric Heaters. This thesis aims at designing a sub-system of these heaters, a highly efficient, megawatt-class, constant impedance tunable power extraction circuit. At resonance, the power extraction circuit extracts the kinetic energy of the modulated electron beam from an RF power source, converts it to electromagnetic energy. Circuit elements like the inductors used in this application exhibit parasitics

like the proximity effect and self-resonance in the bandwidth of our interest, which further enhance the losses and affects the efficiency of the circuit. We model these effects and suggest a new method to approach the design of at such frequencies. We test these methods with experimental measurements and discuss these results. Finally, we propose a multi-stage power extraction circuit based on the limitations of single-stage impedance transformations. We discuss simulation results as a proof of principle.

1.2 History

Earth's atmosphere can be divided into four main layers based on temperature variations [5]. The troposphere extends from the surface of the earth to about 12 km. It is home to all the weather-related activity in the earth's atmosphere. Although variations do occur, the temperature usually decreases with increasing altitude in this layer (40 °C to -60 °C)[6-7]. The stratosphere extends from 12 km to 55 km and the temperature rises with increase in altitude. The ozone layer is within the stratosphere and absorbs the ultraviolet radiation from the sun and hence the increase in temperature (-60 °C to 0 °C)[8]. The mesosphere is the third layer and it roughly extends from 50 km to 85 km. The temperature drops with increasing altitude in this layer and is the coldest place on earth with an average temperature around -85 °C [9]. The thermosphere extends from 80 km to 1000 km and the temperature gradually increases with height within this layer (-85 °C to 1500 °C). Finally, the exosphere roughly ranges from 700 km to 10,000 km above the

earth's surface[10]. The boundaries become increasingly non distinct and hence the overlap between the layers as we travel higher in altitude. We are interested in the ionosphere, a layer that includes the thermosphere and parts of upper mesosphere and lower exosphere. It extends from 60 km to 1,000 km altitude. It is the ionized part of the earth's upper atmosphere. The amount of ionization varies greatly with the amount of radiation received from the Sun. Thus, there is a diurnal (time of day) effect and a seasonal effect. Global navigation systems (GPS/GNSS) use different models to compensate for the ionospheric effects. This makes it extremely attractive for further research to improve shortwave radio propagation (reflection), trans-ionospheric communication(refraction) & navigation systems [11].

The presence of an electrically conducting region in the earth's atmosphere was first postulated by CF Gauss in the year 1839, to account for the observed variations in the earth's magnetic field [12]. In 1926, Scottish physicist Robert Watson-Watt introduced the term ionosphere for the first time to describe the above region [13]. Edward V Appleton was awarded a Nobel prize in 1947 for experimentally confirming the existence of the ionosphere in 1927 [14]. Lloyd Berkner first measured the height and density of the ionosphere and paved the way for a complete theory of short-wave radio propagation. Three distinct layers (D, E & F) are identified in the ionosphere based on the electron density, ionization & recombination rates, and attenuation/absorption of different radio wave signals [14-15]. The D layer is the innermost layer and it absorbs HF waves below 10 MHz to a large degree. HF waves below 10 MHz cause electrons to move faster and collide with neutral molecules and give up their energy. The E layer, also known as the Kennelly-Heavyside layer, is

the middle layer of the ionosphere. They can reflect radio waves lower than 10 MHz [15]. The F layer, also known as the Appleton Barnett layer, is the outermost layer in the ionosphere. It has the highest electron density [14-15] and is responsible for shortwave radio communications . While E and F layers are important for shortwave radio propagation, the D layer is responsible for degradation in trans-ionospheric communication signals.

1.2.1 Ionospheric Modification

Powerful high frequency radio waves can be used to temporarily modify the ionosphere. These controlled, active experiments are useful in studying the upper atmosphere through observations of ionospheric response to high frequency induced perturbations. It is also used for basic physics investigations (studying plasma) [2- 3]. Ionospheric modification was originally used to produce small perturbations in the local ionospheric electron thermal balance. The response of the ionosphere to these induced temperature fluctuations could then be used to study ionospheric heating & cooling processes, chemical reaction rates and collisional cross-sections. Ionospheric heaters, the high-power high frequency transmitting facilities rely on the ability of the ionosphere to reflect the waves back to the surface of the earth for diagnostics.

Geophysically, the state of the ionospheric plasma can be described by four important parameters: electron density, electron and ion temperature, and ionic composition. Radio propagation depends uniquely on electron density. The iono-

spheric plasma can be seen as an optical medium whose refractive index is given by,

$$n = \sqrt{1 - \frac{\omega_p^2}{\omega^2}} \quad (1.1)$$

and the characteristic frequency is,

$$\omega_p = \sqrt{\frac{n_e e^2}{\epsilon_0 m_e}} \quad (1.2)$$

where $\omega, n_e, e, \epsilon_0, m_e$ represent the frequency of the electromagnetic wave, electron density in the medium, electron charge, dielectric constant of free space, and mass of an electron respectively. If the frequency of the electromagnetic wave is lower than the plasma characteristic frequency, we see that the refractive index of plasma is imaginary. If the frequency of the electromagnetic wave is higher than the plasma characteristic frequency, the refractive index is less than unity. Hence, the electromagnetic waves with its frequency lower than the plasma frequency gets totally reflected while the waves with its frequency higher than the plasma frequency gets transmitted. The former is used in short wave propagation while the latter is used in satellite communication.

1.2.2 Ionospheric Heaters

A handful of Ionospheric heaters exist around the world (see Fig 1.1 & Table 1.1). HAARP in Alaska, EISCAT in Norway, Sura Ionospheric Heating Facility in Russia, Jicamarca Radio Observatory in Peru, Arecibo Ionosphere HF Heater in Puerto Rico and Space Plasma Exploration by Active Radar (SPEAR) in Svalbard are the operational facilities as of April, 2020. The Ionospheric Research Instrument

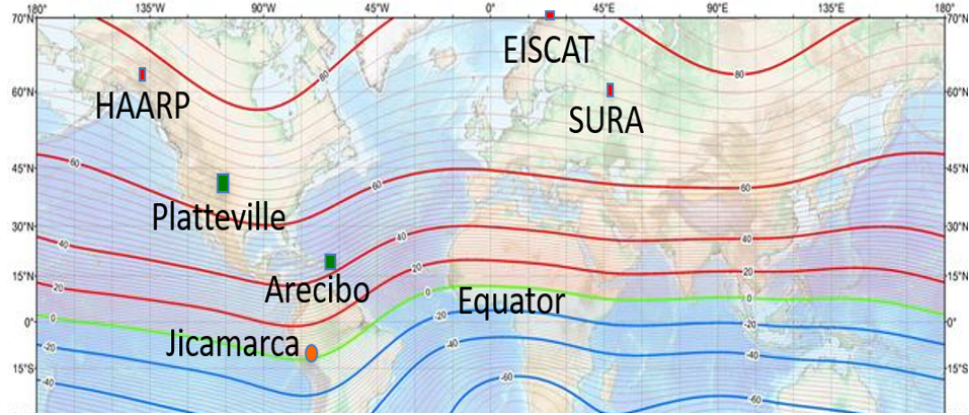


Figure 1.1: Heater facility locations around the world.

(IRI) in HAARP, Alaska directs a 3.6 MW signal, in the 2.8 - 10 MHz region of the HF (high-frequency) band, into the ionosphere. It is a high-power, high-frequency phased array radio transmitter with 180 antennas, disposed in an array that occupies 30 - 40 acres terrestrial area. The Sura Ionospheric Heating Facility consists of three 250 kW broadcasting transmitters in the 4.5 - 9.3 MHz region and 144 crossed dipole antenna array occupying 20 - 25 acres. The Space Plasma Exploration by Active Radar (SPEAR), Svalbard consists of 48, 4kW solid state transmitters in the 4-6 MHz region arranged in 4×6 array of crossed dipoles [16].

All the above mentioned heating facilities pose serious challenge to the study of ionosphere at different application regions as they are permanent installation facilities. Past IM experiments conducted at high latitudes have indicated strong dependence of ionospheric processes on geomagnetic latitude. For example, research has indicated a major advantage to utilizing locations in the dip-equator. Even if they were movable, the sheer size of these antenna systems (20 - 40 acres) are an

<i>Heater Facility</i>	<i>Location</i>	<i>Frequency (MHz)</i>	<i>Power (MW)</i>
High Frequency Active Auroral Research Program, (HAARP)	<i>Gakona, Alaska</i>	2.7 – 10.0	3.6
European Incoherent Scatter Scientific Association, (EISCAT)	<i>Longyearbyen, Norway</i>	3.9 – 8.0	1.2
Sura Ionospheric Heating Facility	<i>Vasilsursk, Russia</i>	4.5 – 9.0	0.75
Jicamarca Radio Observatory	<i>Lima, Peru</i>	49.9	6
Arecibo Observatory	<i>Arecibo, PuertoRico</i>	5.125, 8.125	0.6

Table 1.1: Ionospheric heater facilities around the world.

impractical solution for transportation. A new design to reduce the size of the antenna system necessitates a novel design of the RF power source too. This is to ensure the delivery of an Effective Radiated Power (ERP) to the ionosphere comparable with these existing systems. Hence, the design of a mobile ionospheric heater needs a complete rethink of the RF power source, extraction circuit and antenna systems which cannot reuse previously developed systems.

1.3 Mobile Ionospheric Heaters

Mobile Ionospheric Heaters need a new class of RF power sources at the megawatt level that operate in the 3 -10 MHz . These heaters will operate with

an antenna that is roughly 1/100 in area of the HAARP antenna. For example, at HAARP, a 3.6 MW transmitter power yields an ERP of 5.1 GW. So, if our antenna drops by 1/100 in total area, to maintain the same ERP, we need a 360 MW power source! As a part of a multi-university research initiative (MURI), University of Maryland researched a powerful RF source utilizing Inductive Output Tube (IOT) technology running in class-D amplifier mode. This technology was chosen because it has the potential to operate at high efficiencies. Texas Tech University developed the antenna system for these facilities. In the following sections, we will discuss the RF power source and power extraction circuit in more detail.

1.3.1 RF Power Source

RF sources (Amplifiers) can be classified into Class A, B, C & D amplifiers. While class A, B & C are used for analog designs, class D is used in switching designs. The classes are related to the time period that the active amplifier device is passing current, expressed as a fraction of the period of a signal waveform applied to the input. Theoretical power efficiencies are the lowest in class A and highest in class D systems. Our research effort at the University of Maryland is directed towards building a high power, high efficiency class D, RF source that operates in the 3 - 10 MHz region.

IOTs show promise, both on the high power and high efficiency front. The IOT is a linear-beam vacuum tube, used as a power amplifier for ultra high frequency (UHF) radio waves (commonly found in UHF television transmitters). It typically

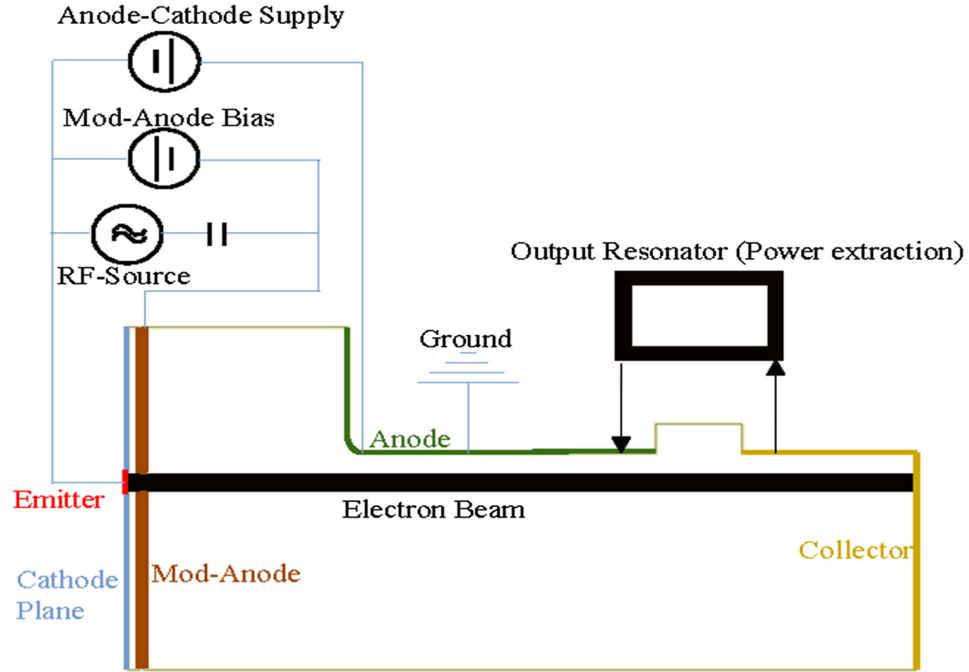


Figure 1.2: Schematic view of the IOT and its circuitry.

operates in class B and class C mode with a frequency range of 200 MHz - 1300 MHz [17]. However, we need higher efficiency and lower frequency range for our application. Specifically, we consider a grid less version of the IOT with several features to enhance efficiency. In this device, an electron beam is accelerated from the cathode and fully modulated by an electrode (mod anode) near the cathode as shown in Fig 1.2. Use of mod anode removes the loss of power due to electron beam interception by grid elements. This is a very important factor limiting the IOT power in high average power regimes. This produces an alternating current that excites a resonant circuit. Figure 1.3 shows the plot of the mod anode voltage and the beam current as function of time. The beam is annular and so the electrons passing through the device experience nearly the same accelerating and decelerating

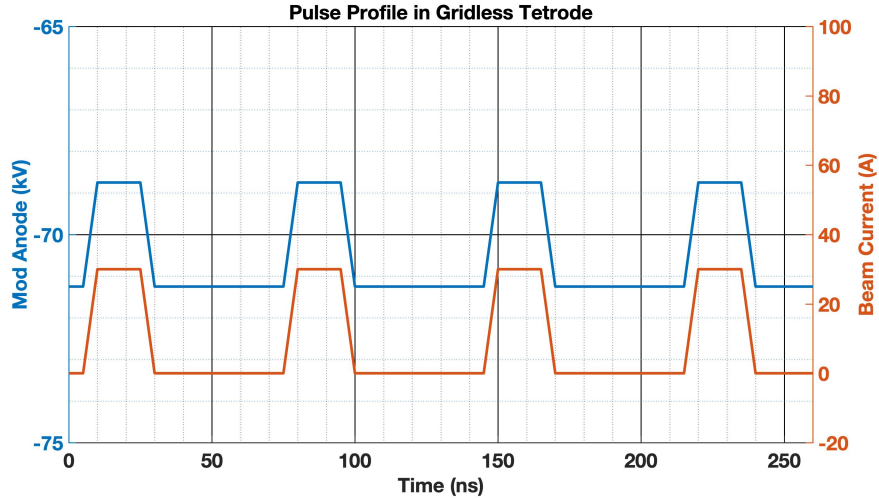


Figure 1.3: Mod anode voltage (blue) and the Beam current (red) as function of time. When the mode anode voltage is positive compared to emitter, beam current is ON.

fields. Electrons emitted from the cathode and accelerating towards the grounded anode, pass through a decelerating gap across which the RF field appears before being collected by a collection surface. This collected current returns to the ground through an energy extraction circuit.

1.3.2 Power Extraction Circuit

The power extraction circuit in the RF device under study converts the kinetic energy of a temporally modulated electron beam into electromagnetic energy. The beam is collected on an electrode surface and the resulting current is passed through the circuit. The circuit generates a potential in response to the current, and that potential is used to decelerate the beam. The circuit must be tunable to cover the desired broad frequency range (3 -10 MHz), and the decelerating voltage should be

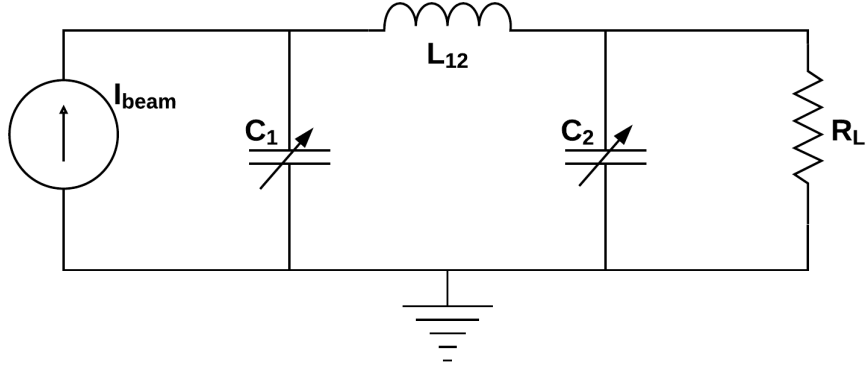


Figure 1.4: Circuit diagram of the pi-circuit used for the power extraction from the IOT.

independent of frequency to maintain high efficiency.

In this relatively low frequency range lumped element circuits are considered instead of cavities given the size limitations imposed. To achieve high power a high voltage beam is required. Consequently, matching the relatively high electron beam impedance ($5 \text{ k}\Omega$) to the load antenna (50Ω) creates situations where high Q resonant circuits are necessary to achieve the high efficiencies required. We design a pi-circuit to achieve the impedance matching and validate the design experimentally.

We initially considered a circuit with a strongly coupled step down transformer and variable capacitors to realize tunability and constant impedance. However, the parasitic capacitance between the input and the output side of the transformer provided a low impedance path for the output current relative to the load. Consequently, significant power dissipated in the primary windings and affected the efficiency of the circuit. [21 - 20].

A pi-circuit consisting of inductors and capacitors (see Figure 1.4) offered the requisite impedance with considerably reduced losses. The circuit shown in Figure 1.4 has a current source that represents the electron beam from the cathode. This current source drives the reactive elements and feeds the resistive load representing an antenna system. While tunability is achieved by varying the capacitor on the input side (C_1), the gap impedance (constant decelerating voltage) is held constant by varying the capacitor on the output side (C_2), keeping the inductor (L_{12}) at a constant value for design simplicity along the frequency band. At resonance, maximum power from the beam is delivered to the resistive load (R_L). We design a pi-circuit to achieve the impedance matching and validate experimentally. E

Although the experiments validate our design hypothesis, measured efficiencies are low because of parasitics in the circuit elements. They exhibit parasitics such as the proximity effect and self-resonance in the frequency range of our interest. These effects further enhance the losses and affect the efficiency of the circuit. We model these effects and test them and find that the errors in the measurements are directly proportional to the Q of the device under test ($Q \sim 2000$). These errors are too large to make any reliable measurements.

Our research finds that the impedance transformation from beam to load (two orders of magnitude) imposes severe restrictions on single-stage design. Additionally, measurements of high Q components aren't very reliable at higher frequencies. We propose a two-stage power extraction circuit that resolves both of these problems. Simulation results show a circuit design that is expected to yield the desired efficiency. The findings from the research in this thesis would help in the even-

tual construction and testing of the MW RF heating system that would facilitate a mobile heater for IM research in the future.

1.4 Goal for the Research

Designing a power extraction circuit for the IOT presents several challenges which will be discussed in the following chapters of this thesis. In chapter 2, we will discuss the design principles in the context of two gun designs: 70kV- 30A gun and 20kV-1A gun. These discussions will identify the various trade-offs one needs to make to achieve high efficiency, constant impedance and tunability. In chapter 3, we will discuss a new method to approach the design of high Q inductors. These discussions are followed by the experiments and measurement limitations for high Q devices. In chapter 4, we discuss the two stage power extraction circuit as a possible solution to our application. Simulation results show a proof of principle. Finally, in chapter 5, we summarize all the results and discuss the advantages and disadvantages of both the circuits and discuss a direction for future projects.

Chapter 2: Power Extraction Circuit for 70 kV-30 A Gun

2.1 Introduction

The power extraction circuit in a tetrode extracts the kinetic energy of a temporally modulated electron beam and converts it into electrical power. This is done by providing an oscillating, decelerating voltage to the electron gun in response to the time dependent beam current. The desired broad operating frequency range (3 - 10 MHz) requires the circuit to be tunable, and the need for a frequency independent decelerating voltage, close to the beam voltage, requires the impedance to be constant as the circuit is tuned.

The RF frequency needed for effective heating (3 - 10 MHz) corresponds to wavelengths of 30 - 100 m. Typically, cavity resonators act as the power extraction circuit in such devices. Figure 2.1 shows a few examples of cavity resonators used at different facilities [19]. The size of these cavities are directly proportional to the wavelength of their operation. Since a cavity's lowest resonant frequency, the fundamental frequency, is that at which the width of the cavity is equal to a half-wavelength ($\lambda/2$), we would need cavities ranging from 15 - 50 m for our application. These cavity dimensions are prohibitive in building mobile ionospheric heaters, where an entire heating system is supposed to be no bigger than 30m - 40m



Figure 2.1: Cavity resonators used in different facilities. (a) Cavities of different sizes. (b) 350 MHz, 4-cell, Nb on Cu. (c) 1300 MHz 9-cell (d) 1500 MHz, 5-cell. Picture Courtesy: Jean Delayen [19]

in dimensions. Hence, a resonant circuit made of lumped element is needed.

In Figure 2.2, an example of a π -circuit design that can achieve the tunability, constant impedance and high efficiency required of the power extraction circuit is shown. The dual requirements of tunability and frequency independent impedance necessitate using two variable elements. Here the tunability is achieved by varying the capacitor on the input side (C_1), the gap impedance is maintained at a constant value by varying the capacitor on the output side (C_2).

Any design begins with a few design goals. The goals of high efficiency, constant impedance, and tunability need to be achieved in the circuit using realizable physical parameters. In the present context, we will set 99 % efficiency in extracting

the incoming power as a design goal that represents high efficiency. Tunability will require the circuit to function in the 3 - 10 MHz region. In order for the over all device efficiency to be in the 90% range, the impedance must be constant within a few percent over the operating frequency range.

To arrive at the needed value of impedance we consider the 70 kV - 30 A gun design, the beam current is a pulsed beam with peak value of $I_{beam} = 30 A$, and has a duty cycle of 25%(class D operation). This current driving the power extraction circuit should develop a 70 kV voltage. Extracting the first harmonic from the pulse using Fourier series,

$$I_1 = \frac{2}{\pi} \left(I_b \sin(\pi/4) \right) = \frac{2}{\pi} \left(30 \sin(\pi/4) \right) = 13.51A \quad (2.1)$$

Therefore, the circuit impedance should be

$$|Z_{gap}| = \left| \frac{V_{RF}}{I_1} \right| = \frac{70kV}{13.51A} = 5.18k\Omega, \quad (2.2)$$

to develop a voltage of 70 kV at the gap. This circuit impedance is the gap impedance of the circuit that plays a very important role in the design. We will use both gap impedance (Z_{gap}) or gap admittance ($Y_{gap} = Z_{gap}^{-1}$) for algebraic simplicity.

2.2 Design of a Single Stage π -Circuit

For high efficiency, all power generated at the source (I_{beam}), should be delivered (see Fig 2.2) to the load/antenna (R_L). However, a portion of the power is dissipated in the inductor coil (frequency dependent coil winding resistance, R_{12}).

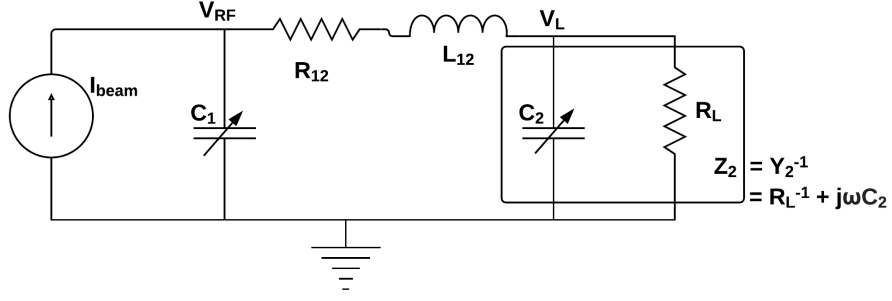


Figure 2.2: Circuit diagram of the π -circuit used for the power extraction from the gridless tetrode.

In this section, we will provide an approximate formula for the ratio power dissipated in the inductor to the power dissipated in the load. To provide a constant decelerating voltage, we will first obtain an expression for the gap admittance and then set the conditions for keeping it a constant at all frequencies in the range of operation. Let the admittance of capacitor C_1 be Y_{C_1} , C_2 be Y_{C_2} , inductor L_{12} be $Y_{L_{12}}$ and antenna/load R_L be Y_L . The admittance looking into the circuit from the source side is the gap admittance we are interested in. The gap admittance is given by,

$$Y_{gap} = Y_{C_1} + \frac{Y_{L_{12}}(Y_{C_2} + Y_L)}{Y_{L_{12}} + (Y_{C_2} + Y_L)} \quad (2.3)$$

At resonance, the circuit presents a real impedance R_{gap} to the source. The power entering the circuit (P_{in}) should be almost entirely delivered to the load resistor (P_L),

$$\frac{|V_{RF}|^2}{R_{gap}} = \frac{|V_L|^2}{R_L} \quad (2.4)$$

where V_{RF} is the decelerating voltage presented to the beam and V_0 is the voltage across the load. Both are complex numbers and the relation applies to their magnitudes. Defining the ratio,

$$\alpha = \sqrt{\frac{R_{gap}}{R_L}}, \quad (2.5)$$

we have,

$$\left| \frac{V_{RF}}{V_L} \right| = \alpha \quad (2.6)$$

The above assumption that the power dissipated in R_{12} is small will put an upper limit on its value, $R_{12} \ll R_L$ where V_L is the voltage across the load. This follows from the fact that the currents flowing through R_L and C_2 add in quadrature, and consequently the current flowing through R_L has a smaller magnitude than the current flowing through R_{12} . Elements Z_2 and the Z_{12} form a voltage divider, consequently

$$\left| \frac{V_{RF}}{V_L} \right| = \left| 1 + \frac{Z_{12}}{Z_2} \right| = \left| 1 + (R_{12} + j\omega L_{12})(R_L^{-1} + j\omega C_2) \right| \quad (2.7)$$

where ω is the angular frequency of operation of the circuit. Since we expect $\alpha \gg 1$, and $R_{12} \ll \omega L_{12}$, this relation gives,

$$\alpha^2 \simeq \left(\frac{\omega L_{12}}{R_L} \right)^2 + (1 - \omega^2 L_{12} C_2)^2. \quad (2.8)$$

The current through the capacitor C_2 and load R_L is given by,

$$I_{C_2} = j\omega C_2 V_0 \quad \text{and} \quad I_{R_L} = \frac{V_L}{R_L} \quad (2.9)$$

Therefore,

$$I_{R_L} + I_{C_2} = V_L \left(\frac{1}{R_L} + j\omega C_2 \right) \quad (2.10)$$

However, this is also the current that flows through the inductor Z_{12} . Hence,

$$I_{Z_{12}} = I_{R_L} + I_{C_2} = V_L \left(\frac{1}{R_L} + j\omega C_2 \right) \quad (2.11)$$

The power dissipated in R_{12} is therefore given by,

$$P_{12} = |I_{Z_{12}}|^2 R_{12} = \frac{V_L^2 R_{12}}{R_L^2} \left(1 + (\omega C_2 R_L)^2 \right) \quad (2.12)$$

The power dissipated in R_L is given by,

$$P_L = I_{R_L}^2 R_L. \quad (2.13)$$

The ratio of the power dissipated in R_{12} to the power dissipated in R_L is therefore,

$$\frac{P_{12}}{P_L} = \frac{R_{12}}{R_L} \left(1 + (\omega R_L C_2)^2 \right) \quad (2.14)$$

Dividing the Eq 2.8 by α^2 and rearranging the terms, we have

$$\left(\frac{\omega L_{12}}{\alpha R_L} \right)^2 = 1 - \left(\frac{1}{\alpha} - \frac{\omega^2 L_{12} C_2}{\alpha} \right)^2. \quad (2.15)$$

Using Eq 2.15, we can rewrite Eq 2.14 as

$$\frac{P_{12}}{P_L} = \frac{R_{12}}{R_L} \left(\frac{1 - (1/\alpha - \omega^2 L_{12} C_2/\alpha)^2 + (\omega^2 L_{12} C_2/\alpha)^2}{1 - (1/\alpha - \omega^2 L_{12} C_2/\alpha)^2} \right) \quad (2.16)$$

As we expect $\alpha \gg 1$, we can safely ignore the $1/\alpha$ term in Eq 2.15 and Eq 2.16 and obtain

$$\left(\frac{\omega L_{12}}{\alpha R_L} \right)^2 = 1 - (\omega^2 L_{12} C_2/\alpha)^2 \quad (2.17)$$

and

$$\frac{P_{12}}{P_L} = \frac{R_{12}}{R_L} \left(\frac{1}{1 - (\omega^2 L_{12} C_2/\alpha)^2} \right) \quad (2.18)$$

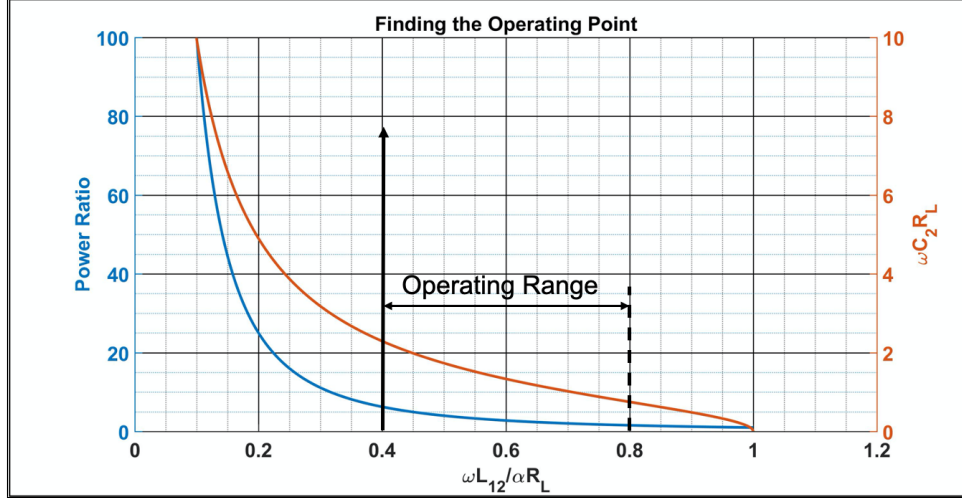


Figure 2.3: Plot of Power Ratio v/s $\omega L_{12}/(\alpha R_L)$ (blue line) . Plot of $\omega C_2 R_L$ v/s $\omega L_{12}/(\alpha R_L)$ (red line)

Thus, using Eq 2.17 and Eq 2.18 we can write the dissipation ratio as,

$$\frac{P_{12}}{P_L} = \frac{R_{12}}{R_L} \left(\frac{\omega L_{12}}{\alpha R_L} \right)^{-2} = \frac{R_{12}}{R_L} \xi^{-2} \quad (2.19)$$

where ξ can be defined as the *Operating Point* of the system and ξ^{-2} is the *Power Ratio*. The significance of ξ is that keeping the power dissipated in the inductor well below the power sent to the load requires both low resistance in the inductor and a not too small ξ .

In Figure 2.3 we plot power ratio as a function of the operating point (blue line). We also plot $\omega C_2 R_L$ as a function of the operating point (red line) using Eq 2.19 and Eq 2.14. For a single inductor coil used in the circuit, operating over an octave, say from $\omega L_{12}/\alpha R_L = 0.4$ to 0.8, is reasonable. The needed capacitance will vary by a factor of about 4 and the power ratio will be below 10. However, if one attempts to increase the range $\omega L_{12}/\alpha R_L = 0.2$ to 0.8, at the low frequency end the

power ratio goes up to about 30 and the range of capacitance needed is factor of 16. These are undesirable for high efficiency and practically realizable circuits. By choosing to operate between 0.4 and 0.8, the tuning range for frequency becomes limited. This is a design trade-off we have to deal with if we use a single inductor coil. Using a variable inductor or switching inductors contributes substantially to contact resistances which can again increase the power dissipation. Thus, in a single stage power extraction circuit, a single inductor is used in the design to obtain high efficiency. Table 2.1 summarizes the ideal circuit parameters for highly efficient power extraction circuit for the 70 kV - 30 A gun configuration at 3 MHz.

R_{gap} ($k\Omega$)	R_L (Ω)	Resonant Frequency (MHz)	$\omega L_{12}/(R_L\alpha)$	$\omega C_2 R_L$	Power Ratio
5.18	50	3	0.4	2.29	6.25
70kV – 30A Circuit	C_1 (pF)	R_{12} ($m\Omega$)	L_{12} (μH)	C_2 (nF)	R_L (Ω)
Design	259	71.7	10.8	2.43	50

Table 2.1: Ideal parameters (99% efficiency) for 70kV-30 A configuration at 3 MHz

In conclusion, designing a highly efficient circuit is dependent on both: (i) optimal circuit parameters and (ii) an efficient inductor design. Choosing the appropriate circuit parameters can only take us so far as we see in the next section. An efficient inductor design is essential if we need higher efficiencies. Designing and testing good inductors comes with its own advantages and disadvantages. We will

elaborate on this in the next chapter. In the next section we discuss some experimental results that show a proof of principle for good circuit design and reasonably high efficiencies.

2.3 Simulations and Cold Test Experiments

R_{gap} ($k\Omega$)	R_L (Ω)	Angular Resonant Frequency(rad/s)	$\omega L_{12}/(R_L\alpha)$ ($F - \Omega - rad/s$)	$\omega C_2 R_L$	Power Ratio	R_{12}/R_L
5.18	50	$2\pi * 3.04 * 10^6$	0.7	1.02	2.04	0.06

Table 2.2: Impedance values for $R_{gap} = 5.18 k\Omega$ and $R_L = 50 \Omega$ for 90 % efficiency.

Given a resonant frequency, gap impedance and load, we pick the values of the other circuit elements using the plot in Figure 2.3. For a load resistance, $R_L = 50\Omega$ and resonant frequency, $f = 3.04$ MHz, the relevant values of $\omega C_2 R_L$, R_{12}/R_L , $\omega L_{12}/(R_L\alpha)$ for 90% efficiency (using Eq 2.19) from the plot are captured in Table 2.3. Using these values, the actual circuit parameters C_1 , C_2 , L_{12} , R_{12} are calculated and recorded in Table 2.3.

Figure 2.4 shows an experimental setup with inductors and capacitors (based

70kV – 30A Design	C_1 (pF)	R_{12} (Ω)	L_{12} (μH)	C_2 (nF)	R_L (Ω)
Simulation	137.4	3	21.3	1.07	50
Experiment	137 ± 1	3.1 ± 0.2	21.3 ± 0.5	1.04 ± 0.03	51.5 ± 0.2

Table 2.3: Circuit Parameters for the 70kV-30A case.



Figure 2.4: Actual experimental π -circuit setup for the 70kV-30A cold test case.

on the above values) connected in the pi fashion. C_1 is a single vacuum variable capacitor (pF range), C_2 is two vacuum variable capacitors connected in parallel (nF range). L_{12} is a the inductor coil and R_L is the 50Ω load connected across C_2 . The input side of circuit is connected to Vector Network Analyzer (VNA) using a coaxial cable. The VNA applies a test voltage to the circuit and measures the reflected voltage to calculate impedance of the device under test (DUT). It can measure the circuit response for a bandwidth of our interest and graph the impedance as a function of the frequency. A PSpice simulation using the above values is conducted to benchmark our cold test experiments [20]. The resultant gap impedance (both real and imaginary) is plotted as a function of frequency in Figure 2.5.

For a 70kV-30A design, the circuit needs to present a gap impedance, $R_{gap} =$

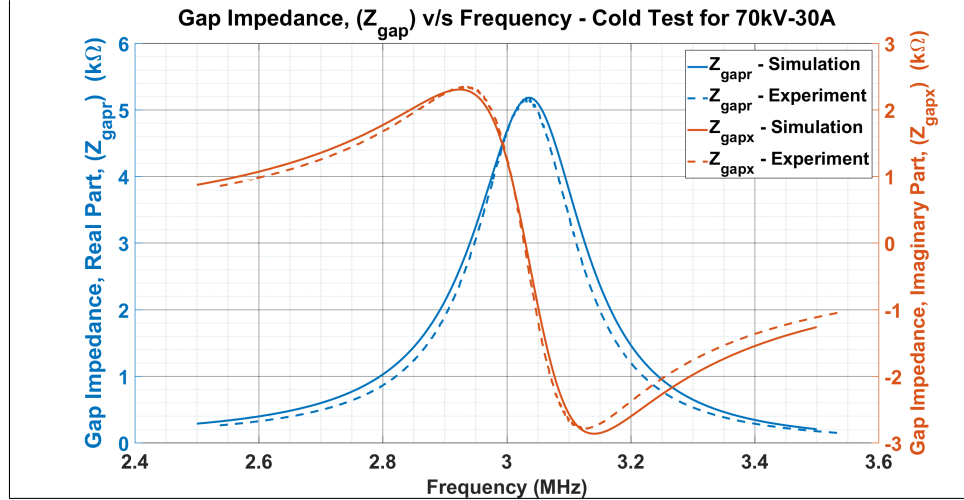


Figure 2.5: Plots for Gap Impedance as a function of Frequency.

$5.18k\Omega$ at resonance. Finally, the resonant frequency, real part of gap impedance at resonance, and efficiency are summarized in Table 2.3. We see a good agreement in impedance from simulation and experiment. However, to make further gains in efficiency, we will have to reduce the winding resistance of the inductor coil. Building a 70kV - 30A gun is beyond the purview of this research (for monetary reasons). We built a π -circuit that was suitable for Naval Research Laboratory (NRL) electron gun that operated between 20 kV- 35kV. In the next section we will look at the results from these experiments.

2.4 Experiments on the NRL Gun

The following section is from the paper titled “Experimental studies on radio frequency sources for ionospheric heaters” published in Physics of Plasma [27] and I co-authored it. A π -circuit was built at the University of Maryland with circuit

Observed Data	Resonant Frequency, f_o (in MHz)	Z_{gap} (Real Part) (in $k\Omega$)	Efficiency, η (in %)
Simulation	3.04	5.28	89.9
Experiment	3.04	5.16	89.3

Table 2.4: Comparison of Data from Simulation and Experiment.

elements and properties that are suitable for the NRL electron gun (shown in Figure 2.6). The NRL gun has a gated and gridded thermionic cathode and was originally designed to operate in the frequency range from 500MHz to 2.5GHz by direct coaxial coupling to the grid. The grid is composed of concentric wires with a radius of 30 μm and placed 1 mm in front of the tungsten dispenser cathode that has a Pierce configuration for a focused beam [28]. The cathode-anode voltage is designed to operate from 20 to 35 kV with a cathode-grid voltage in the range of 10 - 200V, allowing for flexible operation. We were able to drive the grid directly through its biasing electrode (about -30 V relative to the cathode) with square pulses of small duty factor (25%) and a peak voltage of 80V, in the 3-10 MHz RF frequency range.

This experiment is a scaled-down, proof-of-principle testing of the π -circuit to be used as a tunable power extraction device for the bunched electron beam. One of the drawbacks of using the NRL electron gun is that its Pierce gun configuration of the cathode leads to a converging electron beam that comes to a focus shortly after going through the exit hole in the anode. From there, the beam diverges and



Figure 2.6: Power Extraction Circuit and the low power IOT electron gun at NRL. The inductor is made of copper tubing, and the capacitor of the π -circuit sits on top of the gridded gun.

requires a focusing magnetic field to propagate. This is not to be confused with the better design of a magnetically immersed gun guided by a long solenoidal magnetic field.

The electron beam in our experiment propagated through a 24 cm drift section embedded in a short (10 cm) solenoidal magnetic field for beam focusing. The focusing solenoid had 500 turns and could provide 141 G of field at a current of 1A. The diverging beam was mildly focused by the solenoid to be approximately collimated, and it then hit a collector plate isolated from the ground using a high voltage feed through.

The π -circuit used in the experiment was composed of a large core 7-turn inductor, L_{12} of radius 12.2 cm, made from 0.95 cm outer diameter copper tubing, a vacuum variable capacitor (VVC) for C_1 , and two VVCs in parallel for C_2 . The

values for each component are shown in Table 2.4 and 2.4. The output load was 50Ω , and the input RF voltage induced in the π -circuit on C_1 is measured with a 1000:1 voltage divider (ROSS Model VD90-4.1-A-LB-A) into the oscilloscope. The divider is composed of a capacitive/resistive divider, where the input R is $360 \text{ M}\Omega$ and input C is 3.3 pF and the output R is $564 \text{ k}\Omega$ and output C is 2980 pF . The ROSS divider's normal frequency range is from DC to 5 MHz . The output voltage is measured directly on the same oscilloscope after attenuation with high power RF attenuators.

C_1 (pF)	L_{12} (μH)	R_{12} (Ω)	C_2 (nF)	R_L (Ω)
116.8	12.4	2.6	2.7	50

Table 2.5: π -circuit parameters used in the NRL gun at 4.1 MHz

C_1 (pF)	L_{12} (μH)	R_{12} (Ω)	C_2 (nF)	R_L (Ω)
116.8	18.37	1.9	2.7	50

Table 2.6: π -circuit parameters used in the NRL gun at 3.1 MHz

The time dependent electron beam current can only be measured directly on the collector before the π -circuit is connected to it. It is measured using a 50Ω terminator, and the current waveform is recorded on the same oscilloscope. With the π -circuit connected, the current on the collector runs through L_{12} in the π -circuit and returns to the ground through the output load resistor of 50Ω . The DC offset of the output RF voltage is the voltage drop generated by the average

beam current on the load resistor. This DC offset voltage therefore can be used to monitor the average current received by the collector. With the assumption that the current temporal profile does not change with the connection of the π -circuit to the collector, the actual current driving the π -circuit during the experiment can be scaled with this DC offset voltage at the load resistor. The driving RF signal was optically relayed to a high voltage pulser floating at the cathode voltage. The output of the HV pulser was connected in series with the biasing DC voltage source and then directly to the bias electrode for the grid. The overall timing of the experiment was provided by a Stanford Delay Generator (Model 535) which also externally triggered the oscilloscope. The voltage and current profiles on the oscilloscope were therefore synchronized in time, and their relative phase was determined. The input power to the π -circuit was calculated as the product of the measured induced input RF voltage and the inferred driving current, with the relative phase included. The output power is simply the average of the output RF voltage squared divided by the load resistance. A sweep of frequencies on the grid in optimizing the output power was performed to establish the resonant frequency of the π -circuit. At this resonant frequency, power transfer efficiencies of the π -circuit were calculated from the input and output powers at various C_2 values for different impedance matching of the π -circuit to the electron beam. The intrinsic values of the capacitance for C_1 and C_2 , the inductance for L_{12} , and the internal resistance of R_{12} were measured using an LCR meter at a frequency of 10 kHz. High frequency properties such as the internal capacitance C_{12} and R_{12} were established by studying the behaviors of the inductor near its self-resonance using a signal generator.

2.4.1 Results

In order to maximize the beam current collected onto the collector, the solenoid field was swept to determine an operating point for the solenoid. The optimal operating point for the solenoid was 1.8 A, collecting a beam current of 0.98 A. After this, the resistor that connects the collector to the ground (used to measure current) was removed and the π -circuit was connected. The power entering the π -circuit, P_{in} , was estimated from the phased product of the alternating Voltage V_{in} and the alternating beam current inferred I_{beam} . The voltage was measured directly, but the alternating beam current was measured separately as described earlier. We did measure the DC component of the beam current with the π -circuit connected using the DC offset observed on the load resistor. The DC current with the π -circuit connected was reduced from that measured with the resistor connected. We attribute the reduction in the total current entering the π -circuit due to the collector charging up to a sufficiently high potential relative to the grounded pipe walls, and this causes some of the electrons to be deflected away from the collector, thus reducing the actual total current entering the π -circuit, as opposed to the measured current when the 50 Ω resistor is connected to the collector and the π -circuit is disconnected.

The measured RF voltage (V_{in}) induced on the input capacitor C_1 of the π -circuit is shown as the blue curves in Figure 2.7(a) for C_2 of 2.7 nF (near maximum output power). The red curve is the simulation result that will be discussed in next section. The V_{in} waveform has an envelope that increases over several microseconds

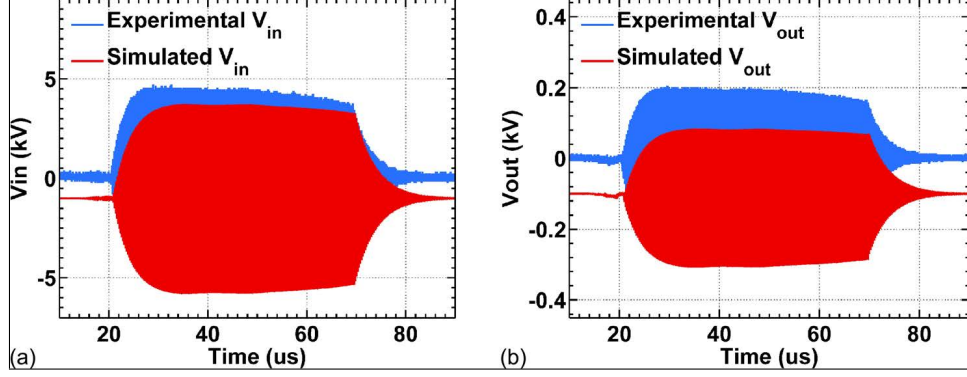


Figure 2.7: Measured (blue) and simulated (red) V_{in} (a) and V_{out} (b) versus time from the π -circuit. For comparisons, V_{in} and V_{out} simulations are displaced by 1 kV and 0.1 kV, respectively.

and decays similarly when the drive RF pulses have ended. The rise and fall times of the envelope are related to the Q-factor of the π -circuit where the power loss is from both the power in the output resistor and the internal resistance of the inductor. Similarly, the measured output RF voltage V_{out} is shown as the blue curve in Figure 2.7(b).

A magnified view of the input RF voltage V_{in} and the input current I_{beam} profile is shown in Figure 2.8 indicating that there is a phase lag between the voltage waveform and the current waveform. This phase lag affects the calculation of input power from the multiplicative product of the voltage and current waveforms at the input capacitor. The output power P_{out} is inferred from the measurement of the voltage across the output 50Ω resistor. The power was optimized by sweeping the frequency of the drive RF in the experiment and observing the maximum V_{in} and V_{out} , obtaining the 4.09 MHz resonant frequency, as was similarly done [29]. The solenoid current was fixed, and we varied the capacitance of C_2 . This would test the

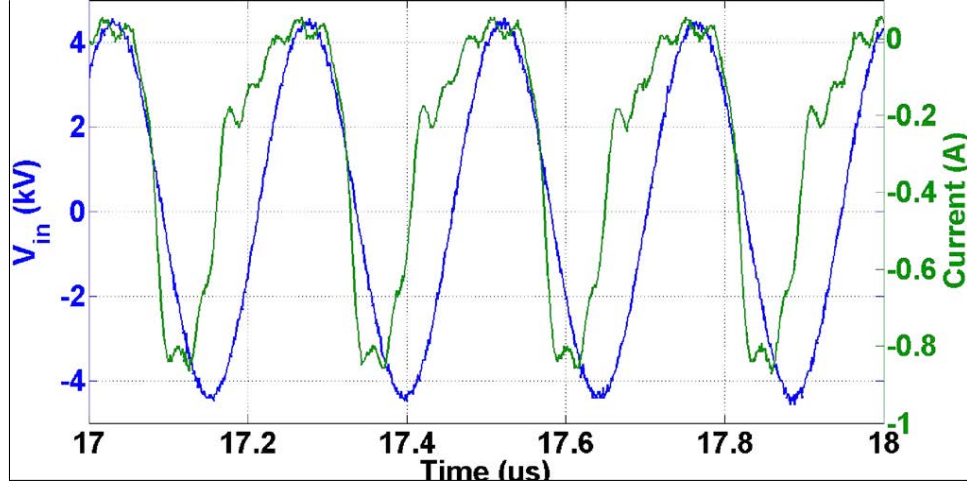


Figure 2.8: $V_{in}(t)$ at a capacitance C_2 of 2.7 nF, an RF drive frequency of 4.09 MHz (blue), $I_{beam}(t)$ measured as a voltage across 50Ω connected to the collector and with the π -circuit removed, a solenoid current of 1.8 A, and an RF drive frequency of 4.09 MHz (green).

influence of circuit impedance as changed by varying C_2 on the circuit performance. Also, by varying C_2 , we are varying the induced V_{in} and consequentially extracting as much kinetic energy from the beam as possible. Figure 2.9(a) shows the input and output powers, and Figure 2.9(b) shows the efficiency inferred at various capacitances for C_2 , at an RF drive frequency of 4.09 MHz. When the capacitor C_2 was varied from 1.5 to 2.7 nF, the input and output power changed, where the output power peaked between 2.3 and 2.5 nF, corresponding to a circuit efficiency (Figure 2.9(b)) of 70%-63%.

This observation of power transfer and transfer efficiency was tested at another frequency of operation to observe any frequency dependence. The resonant frequency of the circuit was lowered to 3.1 MHz by increasing the inductance of the L_{12} inductor. In Figure 2.10(a), the input RF voltage V_{in} is shown as the blue

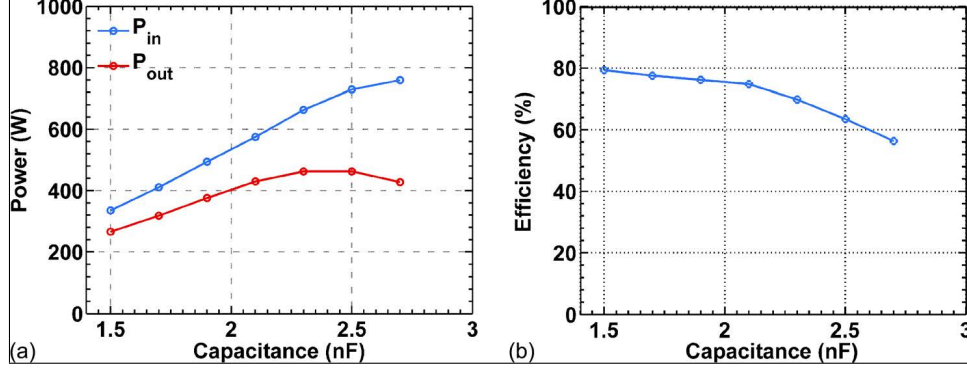


Figure 2.9: Measured (blue) and simulated (red) V_{in} and V_{out} versus time from the π -circuit. For comparisons, V_{in} and V_{out} simulations are displaced by 1 kV and 0.1 kV, respectively.

curve, while the output RF voltage V_{out} is similarly shown as the blue curve in Figure 2.10(b), for both C_2 of 2.7 nF (near maximum output power). The red curve is the simulation result that will be discussed in next section.

A magnified view of the input RF voltage V_{in} and the input current I_{beam} profile is shown in Figure 2.11 at this frequency, illustrating the phase lag between the voltage waveform and the current waveform. Figure 2.12(a) illustrates the input and output power and Figure 2.12(b) illustrates the efficiency measured at various capacitances for C_2 at an RF drive frequency of 3.1 MHz. At 3.1 MHz, the output power peaked between 3.1 and 3.3 nF, corresponding to a circuit efficiency of 60%-56%. When the circuit was operated at 4.09 MHz, its efficiency (see Figure 2.9(b)) was between 70% and 63%.

One should note that the overall input power in the 3.1 MHz case is higher than the corresponding input power in the 4.09 MHz. Since the input currents for both cases are about the same, the phase lags between the current and voltage in

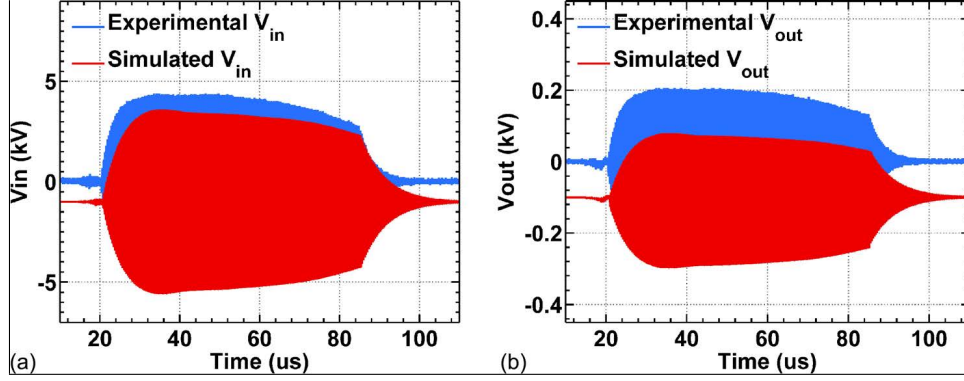


Figure 2.10: Measured (blue) and simulated (red) V_{in} and V_{out} versus time from the π -circuit. For comparisons, V_{in} and V_{out} simulations are displaced by 1 kV and 0.1 kV, respectively.

the two cases are different as is the duty-factor as shown in Figure 2.8 and 2.11.

2.5 Discussion and Conclusion

In order to better understand the model of the π -circuit and its parasitic elements, we compared the simulated V_{in} and V_{out} with experimental V_{in} and V_{out} shown in the previous section for V_{in} in Figure 2.7(a) and for V_{out} in Figure 2.7(b). When the capacitance of C_2 was decreased, the voltage induced on the V_{in} and V_{out} decreased as well and correspondingly the overall power in the circuit, but the transfer efficiency of the circuit increased. This is due to the fact that there is less power stored in the circuit and correspondingly less power being lost in the resistive component of the inductor. When the capacitance C_2 decreases, the circuit has a smaller Q-factor. Figure 2.13 illustrates the measured Q at various capacitances for C_2 at an RF drive frequency of 4.09 MHz. The measured Q of the circuit spans a

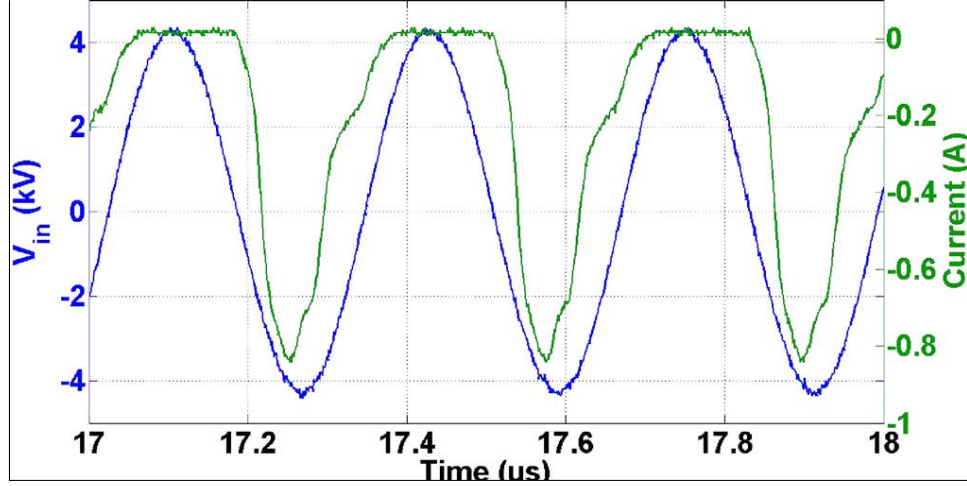


Figure 2.11: $V_{in}(t)$ at a capacitance C_2 of 2.7 nF, an RF drive frequency of 3.1 MHz (blue), $I_{beam}(t)$ measured as a voltage across 50Ω connected to the collector and with the π -circuit removed, a solenoid current of 1.8 A, and an RF drive frequency of 3.1 MHz (green).

range from 23 to 48. Simulations indicate that there is 8.3-15.1A of current through the resistor R_{12} as C_2 is swept over the range, the larger corresponding to the larger C_2 . Sweeping C_2 we vary the induced V_{in} and consequentially extract more kinetic energy from the beam at larger C_2 . PSpice simulations also illustrate that there is a phase shift increase between the current I_{beam} and the induced voltage V_{in} across C_1 with increasing capacitance C_2 .

The measured circuit parameters (C_1 , L_{12} , R_{12} , and C_2) for the π -circuit elements used in the experiment are shown in Table 2.4 for the lower frequency of 3.1 MHz. These same values were used in the simulation. Once again, to better understand the model of the PSpice and its parasitic elements, we compared the simulated V_{in} and V_{out} versus experimental V_{in} and V_{out} shown in Figure 2.10(a) and 2.10(b), respectively, at this lower frequency as well. Similar to the case when

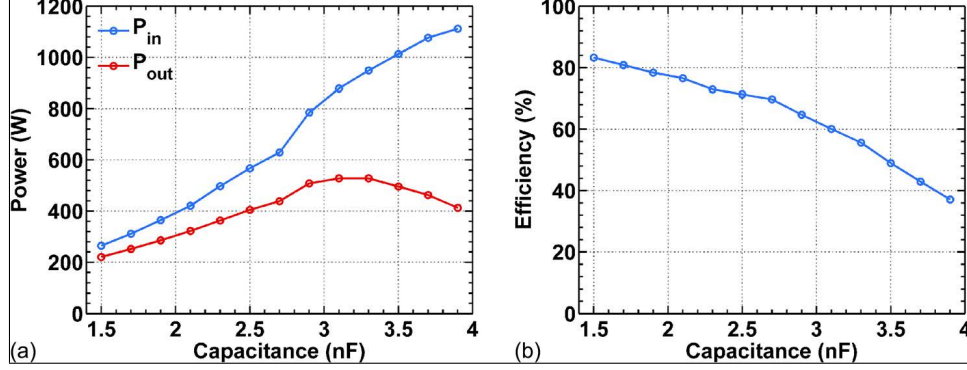


Figure 2.12: Measured (blue) and simulated (red) V_{in} and V_{out} versus time from the π -circuit. For comparisons, V_{in} and V_{out} simulations are displaced by 1 kV and 0.1 kV, respectively.

the operating frequency was 4.09 MHz, as the capacitance C_2 was decreased, the voltage induced on the V_{in} and V_{out} also decreased and correspondingly the overall power in the circuit decreased, but the transfer efficiency of the circuit increased as it did in the 4.09 MHz case. This is due to the fact that there is less power stored in the circuit and correspondingly less power being lost in the resistive component of the inductor. The circuit has a smaller Q-factor when the capacitance C_2 decreases. Figure 2.14 illustrates the measured Q at various capacitances for C_2 at an RF drive frequency of 3.1 MHz. The measured Q of the circuit spans a range from 16 to 76. Simulations indicate that there is 6.5-21.3A of current through the resistor R_{12} as C_2 is swept over the range, the larger corresponding to the larger C_2 . Similarly to the previous case, by sweeping C_2 we varied the induced V_{in} and consequentially extracted more kinetic energy from the beam at larger C_2 .

In conclusion, using a 20 kV-1A electron beam produced by a gridded thermionic electron gun operating in class D mode, we drove an external lumped element power

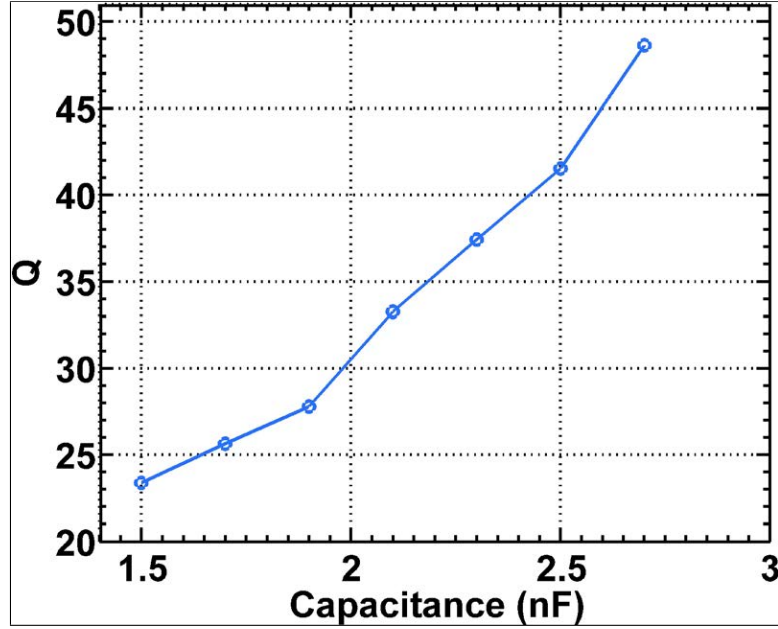


Figure 2.13: Measured Q versus capacitance C_2 at an RF drive frequency of 4.09 MHz

extraction circuit. Detailed analyses of efficiency has showed that we were able to extract at most 84% of the power when the circuit was tuned to have a low Q and as a result low currents in the inductor branch of the circuit, thus dissipating less power in the effective resistance of the inductor. When we tune the π -circuit to maximize output power, the efficiency drops to 60%, and as a result, more power is dissipated in the inductor branch of the circuit due to the fact that the Q has increased, whereas higher energies were extracted out of the beam. In terms of a MW class RF source required for IM research, the required gap impedance Z_{gap} will be significantly lower as compared to the gap impedance needed for the NRL experiment. Calculations and cold test measurements have shown the π -circuit needed for 70 kV-30A device is significantly less sensitive to the parasitic losses in the inductor

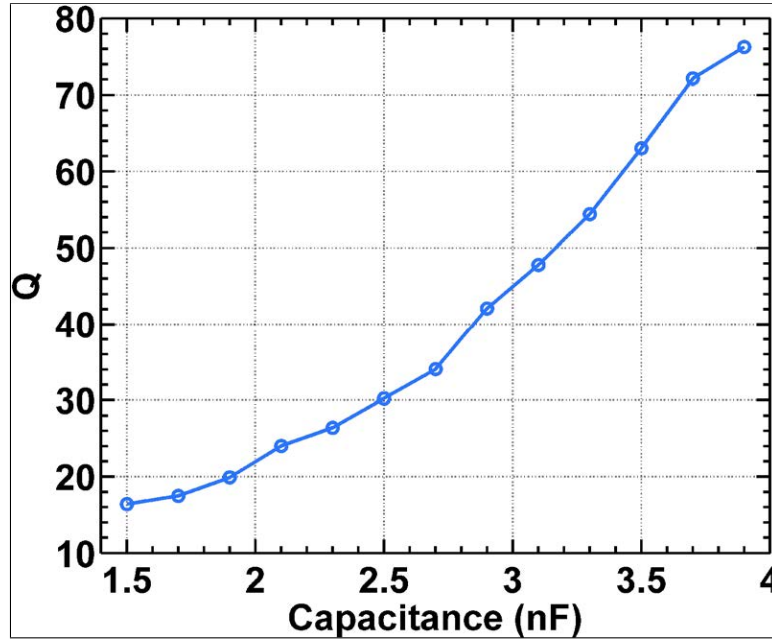


Figure 2.14: Measured Q versus capacitance C_2 at an RF drive frequency of 3.1 MHz

as the beam impedance is substantially smaller [20].

In the next chapter, we develop a method to design high Q inductors essential for low power loss in the power extraction circuit. We design an inductor for 70kV - 30A configuration and experimentally measure these winding resistances and discuss these results.

Chapter 3: Inductor Design: A Novel Approach

3.1 Introduction

The role of the power extraction circuit shown in Figure 3.1 is to convert the kinetic energy associated with the electron beam to electrical energy that can be delivered to a load, in this case an antenna. The circuit acts essentially as a transformer, converting the high voltage, relatively low beam current waveform, to a much lower voltage, higher current waveform that can be carried on a transmission line to the antenna. As the goal for the device is to operate at high efficiency (on the order of 90%), this conversion should take place with minimal loss. That is, the circuit must be designed so as to minimize the power dissipation in the individual elements. Initially, a transformer was considered [21]. However, it was found that the power dissipation in the primary turns of the transformer was excessive, and alternate circuits were considered as will be discussed in this thesis.

Figure 3.1 shows a power extraction circuit in its simplest form: a π -circuit. The electron beam is represented by the current source on the left, the transmission line carrying power to the antenna is represented by the load resistor on the right. The rest of the circuit consists of two capacitors and an inductor with a parasitic series resistance forming the π . The inductor and capacitors form the resonant

circuit that delivers power from the beam (the current source) to the load. The circuit must be resonant because the current waveform from the beam is in the form of a square wave, and the desired output signal is a sine wave. The circuit responds to the square wave by presenting a sine wave voltage to the current source, and driving a sine wave current in the load. If the quality factor of the circuit is high enough, the power to the load contained in harmonics of the driving signal can be minimized. The resonant frequency of the circuit is tuned by varying the capacitors. In the process of tuning the resonant frequency the impedance presented to the current source must be constant, thus two tuning capacitors are required.

Ideally, the reactive elements are passive and lossless and hence transfer all incoming power to the load without any loss. However, these elements have loss in reality. Capacitor losses are relatively smaller and manageable compared with inductor losses. Capacitors generally have dielectric losses and lead connection losses. Dielectric losses are minimized by using vacuum variable capacitors. Thus, the capacitive losses depend only on lead connection losses and can be made negligible by using short conductor leads of sufficient diameter.

Inductors in general have winding losses (both DC & AC) and core losses. We consider only air core inductors. This leads to winding losses in the inductors as the major source of dissipation in the circuit. These losses are due to wire dimensions (DC resistance), frequency (skin effect) and winding geometry (proximity effect). These losses, also called as inductor parasitics, become significant at higher frequencies and contribute to the dissipative losses in the system. Hence a good design of the inductor accounts for all these effects and optimizes them for the highest

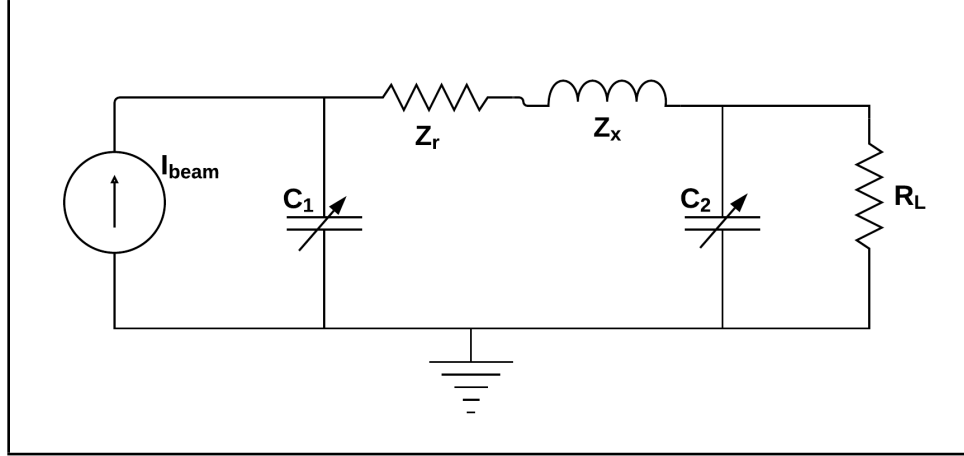


Figure 3.1: A π -circuit as a simple power extraction circuit.

efficiency. In the next few sections, we will develop a theoretical approach to design a highly efficient inductor for our application.

3.2 Inductor Parasitics

At first, we need to establish a quantifiable relationship between inductor losses and efficiency of the circuit. As discussed in the previous chapter, the ratio of power dissipated in the inductor (L_{12}) to the load (R_L) is given by

$$\mathbf{fx} = \frac{P_{12}}{P_L} = \frac{Z_r}{R_L} \xi^{-2}, \quad (3.1)$$

where Z_r is resistive loss in the inductor and ξ is the operating point of the system given by

$$\xi = \frac{Z_x}{\alpha R_L}, \quad (3.2)$$

where α is a constant that represents the square root of the ratio of the impedance seen by the current source and the load resistance. Z_r and Z_x are the resistive and

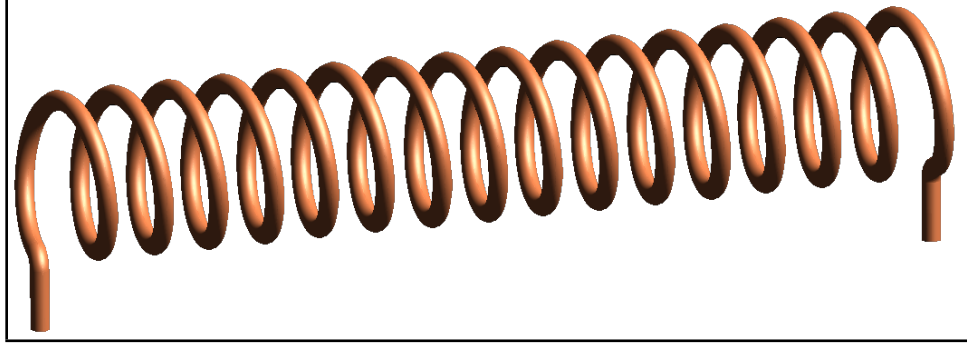


Figure 3.2: A sample solenoidal inductor coil [31]

reactive components of inductor impedance in the π -circuit. For a highly efficient circuit, the power ratio f_x needs to be very small. Ideally, inductors are purely reactive components. The resistive component is due to winding resistance of the inductor material. Further, it is also frequency dependent (skin effect) and geometry dependent (proximity effect). The inductor also exhibits a self resonant frequency and behaves like a transmission line at higher frequencies. For a solenoidal inductor with circular cross section as shown in Figure 3.2, the inductance is given by

$$L_{12} = \frac{\mu_0 N^2 A}{\mathcal{L}} = \frac{\mu_0 N^2 \pi r^2}{\mathcal{L}} \quad (3.3)$$

where, N is the number of turns, r is the cross-sectional radius, \mathcal{L} is the solenoidal length and μ_0 is the permeability of free space. When the turns are closely spaced, the total wire length is given by, $l = 2\pi r N$. Upon substitution, we have

$$L_{12} = \frac{\mu_0 l^2}{4\pi \mathcal{L}} \quad (3.4)$$

Expressing the above as a fraction of the operating frequency (wavelength) and

using the $f = c/\lambda$ relation, we have

$$Z_x = \omega L_{12} = 2\pi f \frac{\mu_0}{4\pi \ell} \left(\frac{l}{\lambda}\right)^2 \lambda^2 = \frac{\sqrt{\mu_0/\epsilon_0}}{2} \left(\frac{l}{\lambda}\right)^2 \left(\frac{\lambda}{\ell}\right). \quad (3.5)$$

Thus, we now have an equation for Z_x in terms of the solenoid length ℓ , wire length l , frequency of operation f , which can be used to estimate the reactive component of inductor. In finding the resistive component, we have

$$Z_r = R_{12} = \frac{\rho l}{A} = \frac{\rho l}{\pi a^2} (DC) \quad (3.6)$$

where ρ is the resistivity of winding material, a is the wire radius. This equation for Z_r provides a winding resistance when the circuit is operating in DC condition. If the circuit starts operating with time varying signals, the equation needs to be revised to include high frequency effects.

3.2.1 Skin Effect

The time varying current in the winding of an inductor coil is not distributed uniformly over the cross section of the winding as is the DC current. If the winding were a perfect conductor, then all the AC current would reside on the surface of the conductor. This is the skin effect [22 - 23]. For an isolated cylindrical conductor the current distributes itself uniformly on the surface. Windings in inductors are not isolated, their currents influence each other, and as a result, the current is not distributed uniformly over the surface of each winding. This is known as the proximity effect and will be treated in the next section. Since the conductivity of a conductor is finite, the current penetrates (diffuses inward) in from the surface of

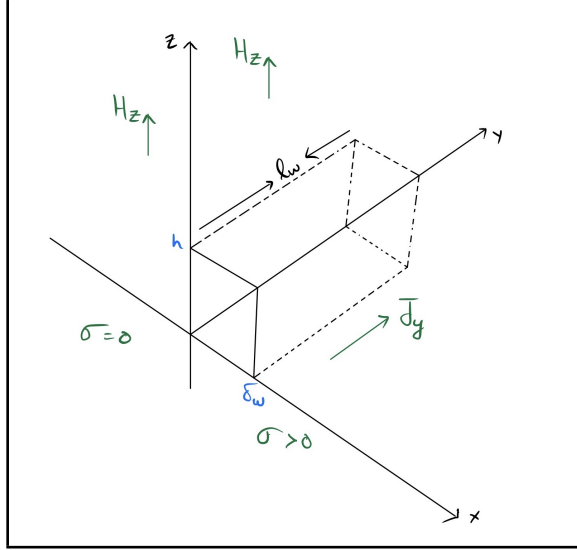


Figure 3.3: Semi-infinite conductor in a magnetic field.

the conductor a small amount known as the skin depth. The skin depth depends on the conductivity of the winding and the frequency of the current as

$$\delta_w = \frac{1}{\sqrt{\pi \mu \sigma f}}. \quad (3.7)$$

Figure 3.3 shows a semi-infinite linear, homogeneous conductor. Let the $y - z$ plane crossing at $x = 0$ form the free space- conductor of conductivity $\sigma = 1/\rho$ with $\sigma \gg \omega\epsilon$. Let us also assume that the magnetic field intensity is sinusoidal in time and has only one component in the z - direction and is a function of x, f, t . Therefore, $\mathbf{H}(x, f, t) = H_m \cos(\omega t) \hat{\mathbf{k}}$ for $x \leq 0$, where $H_m = H_z(0)$ is the amplitude of the magnetic field intensity in free space. The magnetic field intensity in the conductor is described by the *Helmholtz equation* in phasor form.

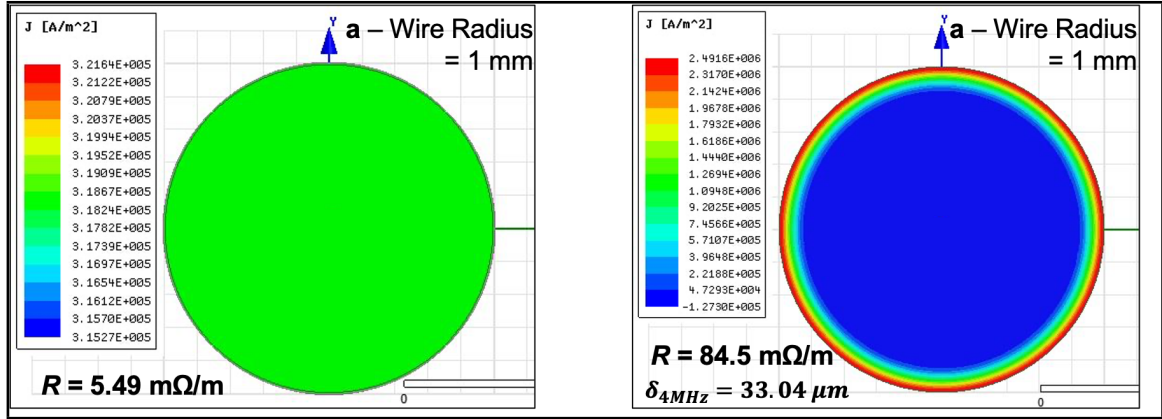


Figure 3.4: Comparison between DC and AC current flow. On the left, DC current flow is uniform in a wire. On the right, the AC current accumulates towards the surface.

$$\frac{d^2 H_z(x)}{dx^2} = j\omega\mu\sigma H_z(x) = \gamma^2 H_z(x) \quad \text{for } x \geq 0 \quad (3.8)$$

where ω is the angular frequency, μ is the permeability and γ is the complex propagation constant given by

$$\gamma^2 = j\omega\mu\sigma. \quad (3.9)$$

The skin depth decreases when frequency increases. Figure 3.4 shows a comparison between a conductor carrying DC current and AC current. In DC, the current flows through the entire surface of the conductor. In AC, the current accumulates more towards the circumference and falls off exponentially deep inside the conductor. Thus, the resistive component in inductor is now estimated using a modification to Eq 3.6 as

$$Z_r = R_{12} = \frac{\rho l}{A} = \frac{\rho l}{2\pi a \delta_w}. \quad (3.10)$$

In the next section, we will discuss proximity effect and how it further enhances

the resistance in the presence of adjacent conductors.

3.2.2 Proximity Effect

The proximity effect in a conductor is caused by the magnetic field induced by current flowing in adjacent conductors [24-25]. The proximity or closeness of other current-carrying conductors affects the ability of the conductor to carry high-frequency current. Each conductor is subjected to its own field and the fields generated by other conductors. The situation is best understood considering first the case of perfectly conducting wires. In this case current flows only on the surface of a conductor and the magnetic field is tangent to the surface and proportional to the local surface current density. The integral of the dot product of the magnetic field and the path element following a path encircling the winding gives, by Ampere's Law, the total current in the winding. The surface current distribution is affected by the currents in other windings, but the total current carried by a winding is fixed. Power dissipation, which is proportional to the square of the current density, will be minimum when the current is uniformly distributed. This is the case of an isolated winding. When the effect of other windings comes in to play, the current density is nonuniform on the surface, and power dissipation and resistance go up.

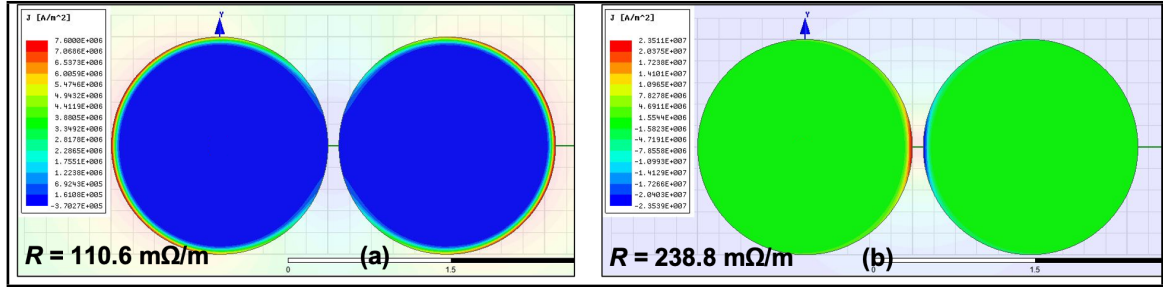


Figure 3.5: Proximity Effect: (a) current flowing in the same direction
(b) current flowing in the opposite direction

The proximity effect causes nonuniform current density in the cross section of conductors, increasing significantly the winding loss at high frequencies. When two or more conductors are brought into close proximity, their magnetic fields may add or subtract. The high-frequency current will concentrate within a conductor, where the magnetic fields are additive. The proximity effect in inductors and transformers is caused by the time-varying magnetic fields arising from currents flowing in adjacent windings. Figure 3.5 shows a comparison of current flowing in two adjacent conductors in the same direction and in opposite directions. It is noteworthy to compare and contrast the enhancement in resistance due to skin effect and proximity effect. Thus, the magnitude of the proximity effect depends on (i) conductor geometry (shape and size), (ii) arrangement of conductors, and (iii) spacing. Mathematically, the proximity effect is very complex. A rigorous mathematical treatment can be found in [26]. However, we use the 2D software simulations (ANSYS Maxwell) of inductor coils to estimate the enhancement in the resistive component due to proximity effect.

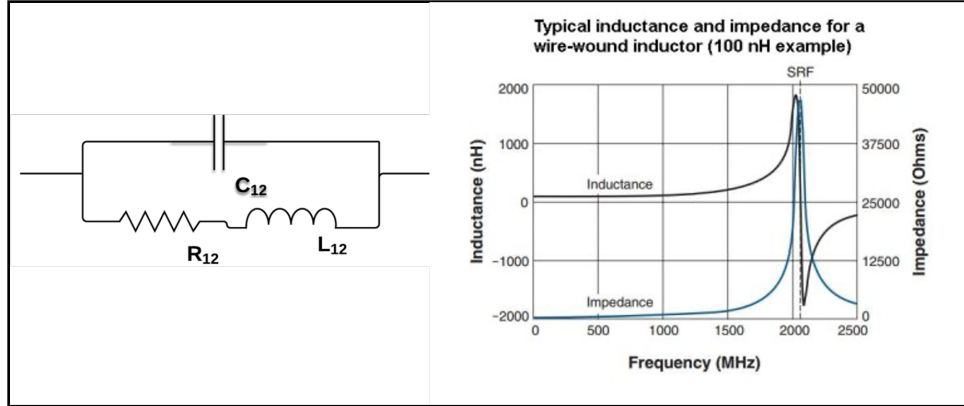


Figure 3.6: A simple parasitic model of the inductor (left). Inductance (black) and impedance (blue) plot as a function of frequency for typical inductor (right). Above the SRF, the coil behaves as a capacitor

3.2.3 Self Resonance

The self-resonant frequency (SRF) of an inductor is the frequency at which the parasitic capacitance of the inductor combines essentially in parallel with the inductance of the inductor resulting in an extremely high impedance. At this frequency the device looks like an open circuit (see Figure 3.6). This phenomenon can also be understood in the case of a single layer solenoid by considering the inductor to be a helical transmission line. In this case the impedance will diverge when the transmission line is a quarter wavelength long. If we approximate the propagation path to be the length of the winding then resonance will occur when $l = \lambda/4$. We will use this as an upper limit for the length of the windings in our designs presented in the next sections.

3.3 Modelling Proximity Effect in Inductors

A 2-D ANSYS Maxwell simulation of inductor coils will help us evaluate the enhancement in resistance of the coil due to the proximity effect [30]. An inductor coil in 2-D can be visualized as shown in Figure 3.7.

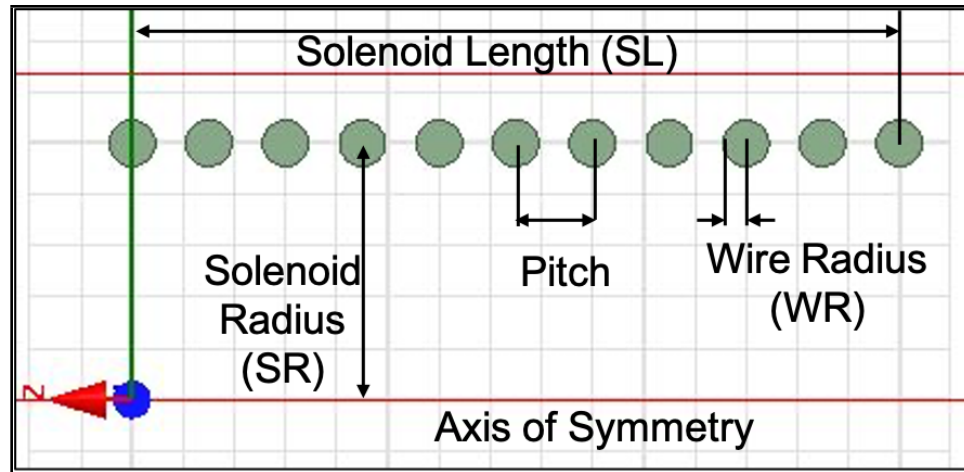


Figure 3.7: A 2D Ansys Maxwell simulation example to explain different variables and boundaries.

It shows all the conductors that carry current in the same direction and an axis of symmetry. Let us define a few terms in this context. Solenoidal length, SL is the length of the coil. Solenoidal Radius, SR is measured from the center of any conductor to the axis of the symmetry. *Pitch* is the center to center distance between two adjacent turns. Wire Radius, WR is the radius of the conductor used in the simulation. We apply a current source of 1A to all the conductors as an initial condition and enforce symmetric boundary condition on the axis (to simulate the other half of the coil) and balloon boundary condition on the remaining boundaries

to isolate the model from other sources of current or magnetic fields. The ANSYS Maxwell solver determines the electric and magnetic field quantities and we use them to find the resistance of the coil. The current distribution in each of the conductors is different from the others due to the proximity effect.

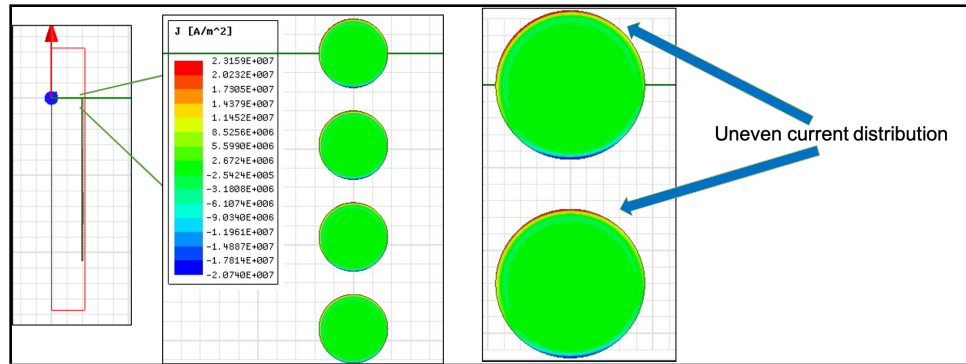


Figure 3.8: Conductors at the edge of solenoidal coil have non uniform current densities

While the conductors at the edge of the coil have higher current densities that accumulate at the outer edges (see Figure 3.8), the conductors at the center have relatively uniform (see Figure 3.9) current densities around their edges. At the center of the coil, the conductors experience a symmetric magnetic field penetration (conductors exist on both sides) and thus have a relatively uniform current distribution. At the edge of the coil, the conductors experience asymmetric magnetic fields, have nonuniform surface current densities, and hence show higher resistances.

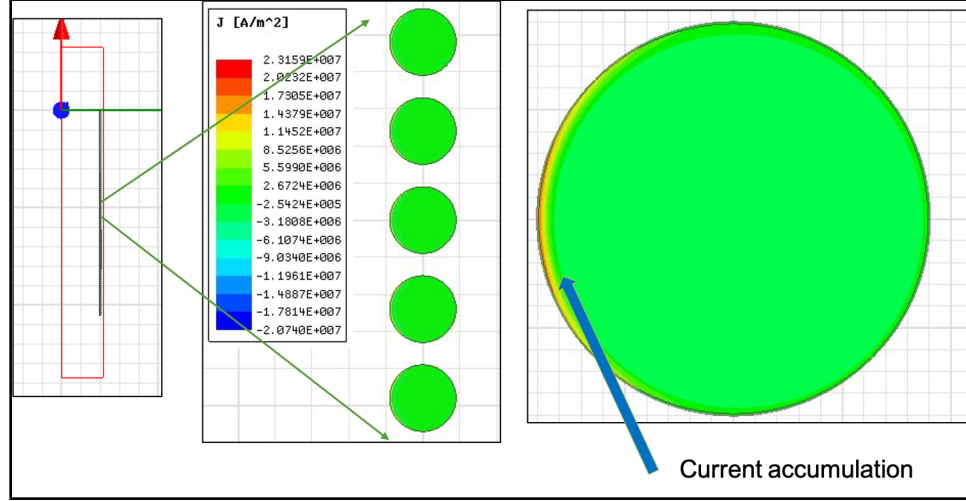


Figure 3.9: Conductors at the centre of solenoidal coil have a relatively uniform current distribution

We know that power dissipation in the conductor is given by,

$$P = \frac{dW}{dt} = \frac{1}{2} \int_V \mathbf{Re}(\mathbf{E} \cdot \mathbf{J}^*) d\tau \quad (3.11)$$

where \mathbf{E} is the electric field and \mathbf{J}^* is the complex conjugate of the current density in these conductors. The resistance of each conductor is given by,

$$R_{prox} = \frac{P}{I_{rms}^2} \quad (3.12)$$

We have set $I_{peak} = 1A$. Hence, $I_{rms} = \frac{I_{peak}}{\sqrt{2}}$. Therefore,

$$R_{prox} = 2 \cdot P \quad (3.13)$$

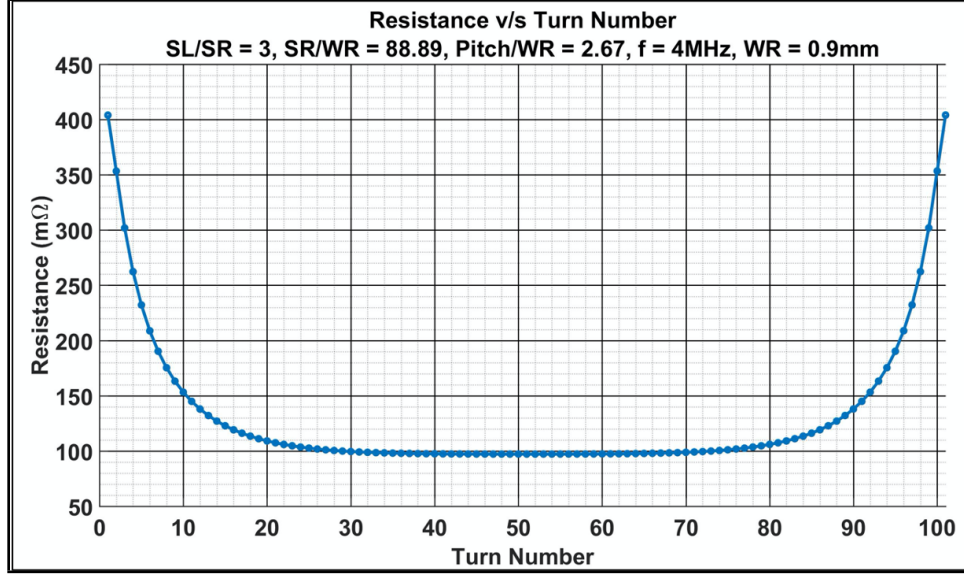


Figure 3.10: Resistance as a function of the Turn Number for an inductor coil of turns, $N = 101$, $SL = 24cm$, $SR = 8cm$, $WR = 0.9mm$, $Pitch = 2.4mm$, at a frequency, $f = 4MHz$

We now have the formula for resistance in each conductor in terms of the fields that the simulation calculates. Figure 3.10 plots the resistance as a function of the turn number (starting from the conductor on the extreme left as the first and the conductor on extreme right as the last) for an inductor coil of turns, $N = 101$, $SL = 24cm$, $SR = 8cm$, $WR = 0.9mm$, $Pitch = 2.4mm$, at a frequency, $f = 4MHz$. We can also estimate the skin effect in each of these conductors using the Eq 3.20. We find the enhancement factor due to the proximity effect as given by,

$$EnhancementFactor, \mathbf{E} = \frac{\sum_{i=1}^N R_{prox,i}}{n \sum_{i=1}^N R_{skin,i}} \quad (3.14)$$

where N is the number of turns. Thus, the enhancement factor calculated here is an average over the turns in the coil.

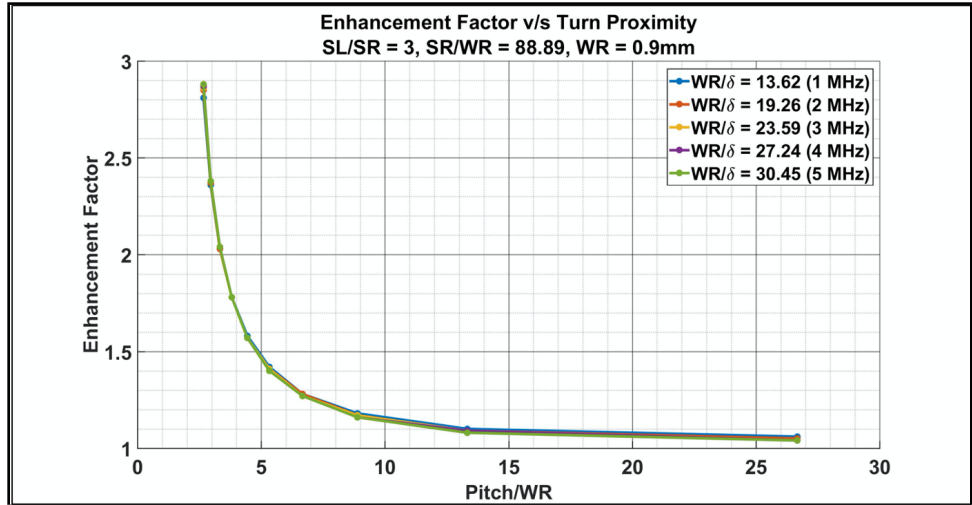


Figure 3.11: E as a function of $Pitch/WR$ for different skin depth ratios

We now have a basic set of equations to estimate the proximity effect. In order to develop an empirical model, we run these simulations as a function of all the variables that are available to us.

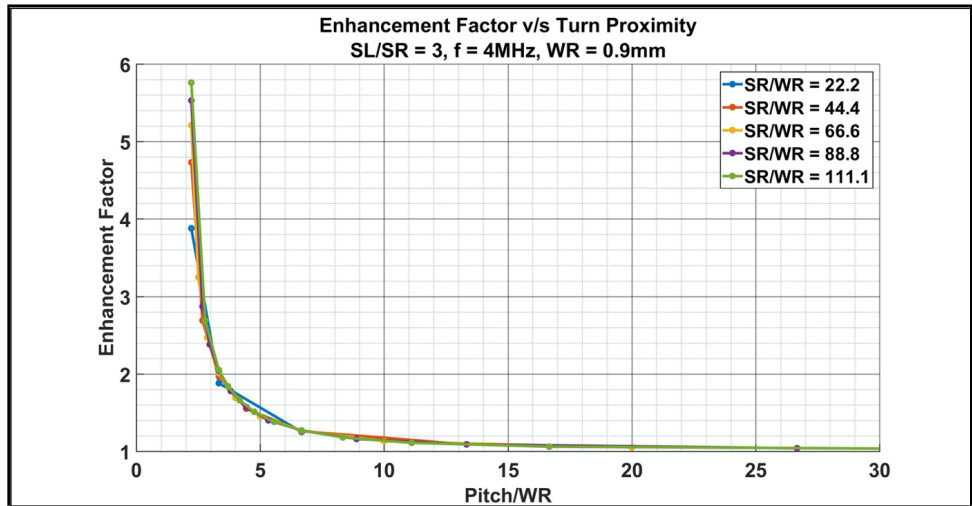


Figure 3.12: E as a function of $Pitch/WR$ for different radii ratios (SR/WR)

Taking the ratios, we plot enhancement factor, E as a function of $Pitch/WR$ for different skin depth ratios (WR/δ_f), radii ratios (SR/WR) and aspect ratios (SL/SR). Choosing a wide range of values for each of these variables gives us a comprehensive data set and curves to estimate resistance using these plots. In Figure 3.11, a plot of the E as a function of $Pitch/WR$ for different skin depth ratios is shown.

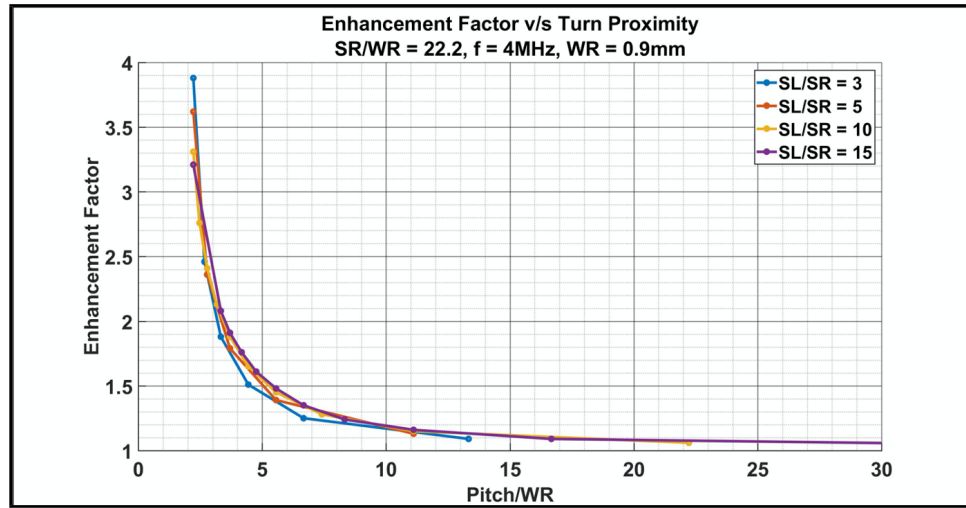


Figure 3.13: E as a function of $Pitch/WR$ for different aspect ratios (SL/SR)

Though the enhancement is primarily dependent on the separation between conductors ($Pitch/WR$), we see that at higher frequencies (or lower skin depths), the resistance does increase when the conductors are very closely spaced. Figure 3.12 plots E as a function of $Pitch/WR$ for different radii ratios (SR/WR). Again, when the turns of the coil are closely wound, the enhancement is significant for higher radii ratio. Finally, we look at Figure 3.13 for a plot of E as a function of $Pitch/WR$ for different aspect ratios (SL/SR). On careful observation, we find that increasing the aspect ratio reduces the enhancement. Thus, we can use the above understanding

to design an inductor for our application. The next section deals with designing one such inductor for a 70 kV - 30 A gun configuration.

3.4 Inductor Design for the 70 kV - 30 A Gun Configuration

In the preceding sections, we have explored the impact of several factors on the impedance of the inductor coil. The above equations and the plots provide us the essential tools to develop an approach to design the inductor. In a 70 kV - 30 A gun configuration operating at 3 MHz, the power extraction circuit should resonate at 3 MHz and transfer all the power from the source side to the load side. The impedance of the circuit at resonance is given by $R_{gap} = 5.18k\Omega$. Note that this impedance has a zero reactance at resonance. For a load, $R_L = 50\Omega$, the resistance ratio, $\alpha = 10.18$. For reasons clearly explained in chapter 2, we choose the operating point of the circuit, $\xi = 0.4$. Hence,

$$L_{12} = \frac{\xi\alpha R_L}{\omega} = 10.18\mu H \quad (3.15)$$

Using Eq 3.5, we can rewrite ξ as,

$$\xi = \frac{\omega L_{12}}{\alpha R_L} = \frac{\sqrt{\mu_0/\epsilon_0}}{2\alpha R_L} \left(\frac{l}{\lambda}\right)^2 \left(\frac{\lambda}{\ell}\right) \quad (3.16)$$

As discussed earlier, to prevent inductor self resonance at the operating frequency, we ensure that the length of wire, $l \ll \lambda/4$. Let us set $l = \lambda/8$ to satisfy the above condition. At 3 MHz,

$$l = \lambda/8 = 12.5m \quad (3.17)$$

Therefore, length of the coil is

$$\mathcal{L} = \frac{\sqrt{\mu_0/\epsilon_0}}{2\alpha R_L} \left(\frac{l}{\lambda}\right)^2 \left(\frac{\lambda}{\xi}\right) = 1.44m \quad (3.18)$$

For high efficiency, we set the ratio of power dissipated in the coil to the load, $f_x = 1\% = 0.01$. So,

$$Z_r = R_{12} \leq f_x R_L \xi^2 = 80m\Omega \quad (3.19)$$

Resistance due to the skin effect is given by,

$$R_{skin} = \frac{\rho l}{2\pi a \delta_w} \quad (3.20)$$

The total resistance due to both skin and proximity effect can be written as,

$$Z_r = R_{12} = E \frac{\rho l}{2\pi a \delta_w} \quad (3.21)$$

where E is the enhancement factor. Using Eq 3.19, we can write

$$\frac{E}{a} \leq \frac{2\pi \delta_w R_{12}}{\rho l} = 89.03 m^{-1} \quad (3.22)$$

As a first order approximation, we can find the lower limit on the wire radius using Eq 3.20 as shown below. If $R_{12} \leq 80m\Omega$, the condition is also true for skin resistance as $R_{skin} \leq 80m\Omega$. Thus,

$$R_{skin} = \frac{\rho l}{2\pi a \delta_w} \leq 80m\Omega \implies a \geq 11.2mm \quad (3.23)$$

Therefore, the wire radius has to be a minimum of 11.2 mm. Let us set the wire radius at a safe margin above the limit to accommodate the proximity effect. Let $a = 15mm$. Rewriting Eq 3.24, we find that,

$$E \leq \frac{2\pi \delta_w R_{12} a}{\rho l} = 1.33 \quad (3.24)$$

Let us pick $E = 1.2$. Using Figure 3.11, we find that the enhancement factor is 1.2 at a $Pitch/WR = 9$. Let us denote pitch by t . Therefore,

$$\frac{t}{WR} = 9 \implies t = 135mm = 13.5cm \quad (3.25)$$

Pitch is also related to the wire length, solenoidal radius and solenoidal length as,

$$t = \frac{2\pi \cdot SR \cdot \mathcal{L}}{l} \implies SR = \frac{t \cdot l}{2\pi \mathcal{L}} = 18.65cm \quad (3.26)$$

Finally, we find the number of turns in the coil, $N = \frac{\mathcal{L}}{t} \cong 11$. Table 3.1 summarizes all the inductor parameters obtained so far. We can see that the resistance, $R_{12} = 71.7m\Omega < 80m\Omega$.

Solenoidal Length, $\mathcal{L} = 1.44$ m	Wire Length, $l = 12.5$ m
Wire Radius, $a = 1.5$ cm	Pitch, $t = 13.5$ cm
Solenoidal Radius, $SR = 18.65$ cm	Turns, $N = 11$
Inductance, $L_{12} = 10.8\mu H$	$R_{12} = 71.7m\Omega$

Table 3.1: Inductor parameters

Hence, we have designed a highly efficient inductor from the ground up starting with a few system parameters. In the next chapter, we will learn how to design a highly efficient power extraction circuit. The inductor design shown in this chapter is an important part of that larger puzzle. In the next section we discuss results from measuring smaller test coils built in the lab.

Solenoidal Length, $\ell = 36.5$ cm	Wire Length, $l = 9.97$ m
Wire Radius, $a = 1.58$ cm	Pitch, $t = 8.39$ mm/
Solenoidal Radius, $SR = 3.65$ cm	Turns, $N = 43.5$
Inductance, $L_{12} = 27.26\mu H$	Pitch/WR, 5.3
SR/WR = 23.17	SL/SR = 10
Enhancement Factor	1.5

Table 3.2: Test inductor used in the lab for measurements

3.5 Measurements on the Test Coils

The inductor coil suitable for a 70 kV - 30 A gun configuration is large (~ 1.4 m long). We begin our tests with coils of smaller dimensions to identify possible issues in measurement. Table 3.2 captures the dimensions of one such inductor built in the lab for testing purposes. We connect the inductor to an impedance analyzer, which measures the unknown impedance by measuring the voltage and current values. While the applied test voltage is known, the current is calculated by measuring the voltage across an accurately known low value resistor. The accuracy of the device is defined by the error in these measurements. Generally, these error margins are directly proportional to the Q of the device under test (DUT). We used a Keysight impedance analyzer and the device manual describes the equations to calculate the errors in measurements. Figure 3.14 plots the absolute value of the measured impedance as a function of frequency. It then identifies the error margins

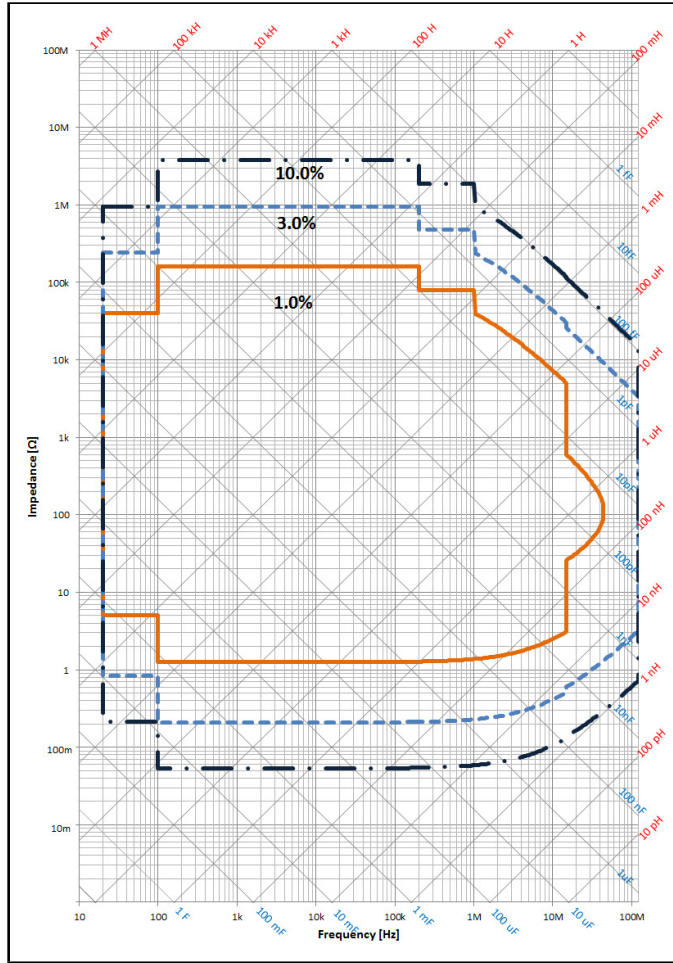


Figure 3.14: Measurement accuracy chart (Source: Keysight Technologies Impedance Analyzer Manual)

(1%, 3%, 10%) for different impedance and frequency ranges.

Table 3.3 captures the predicted and measured impedances at several frequencies. At lower frequencies, we measure impedances in the $m\Omega$ range and in the 10% error margin. At higher frequencies, our error margin reduces to 1% but the absolute value of the measured impedance is dominated by the reactive part (several hundreds of ohms). Hence, even an 1% error translates to several ohms of error on the resistive part. Thus impedance measurements of high Q inductors are limited

Frequency	Z_r (predicted)	Z_r (<i>measured</i>)	Z_x (predicted)	Z_x (<i>measured</i>)
1 kHz	$33m\Omega$	$36.8 \pm 16.7m\Omega$	$171.3m\Omega$	$163 \pm 16.7m\Omega$
5 kHz	$34.19m\Omega$	$43.6 \pm 24.3m\Omega$	$856.4m\Omega$	$808 \pm 24.3m\Omega$
10 kHz	$39.4m\Omega$	$51.3 \pm 16.1m\Omega$	1.71Ω	$1.61 \pm 0.02\Omega$
1 MHz	$394.25m\Omega$	$488 \pm 1590m\Omega$	171.3Ω	$159 \pm 1.59\Omega$
2 MHz	$557.53m\Omega$	$1.17 \pm 3.29m\Omega$	342.6Ω	$329 \pm 3.29\Omega$
3 MHz	$682.92m\Omega$	$1.92 \pm 5.2m\Omega$	513.8Ω	$520 \pm 5.2\Omega$
4 MHz	$788.5m\Omega$	$3.89 \pm 7.47m\Omega$	685.1Ω	$747 \pm 7.47\Omega$

Table 3.3: Predicted and measured impedance values on the test inductor.

by the errors in measurement. High Q devices also make the circuit very sensitive to small changes in ambient properties. In the next chapter, we propose a multi stage power extraction circuit that reduces the high Q requirement on these individual components by dividing the impedance transformation into two stages.

Chapter 4: Design of Two-Stage Power Extraction Circuit

4.1 Introduction

Our single stage power extraction circuit discussed in Chapter 2 and 3 while theoretically feasible, proved to be extremely hard to implement. First, building the circuit elements, in particular the inductors, with the needed resistance in the MHz frequency range was a too stringent task. For example, the inductor that we designed in the Chapter 3 for the 70 kV - 30 A configuration had a Q factor of 2800. Though the design showed that in principle this quality factor could be realized, testing the inductor at higher frequencies became an increasingly difficult task. Past research [32, 33, 33] limit their studies to either kHz frequency range or lower Q factor designs. The best impedance analyzers used to test these elements had an error margin which was directly proportional to the quality factor of the element under test. Thus, it could never be verified that the quality factor specification had been met. Tunability was also an issue with just one fixed inductor. This required the use of variable capacitors with large range of capacitance and at the same time high efficiency. This led us to pursue an alternative approach to designing the power extraction circuit.

Power extraction circuits are essentially impedance transformation circuits

though impedance matching isn't the only task they perform, These lossless circuits transfer power from the source side of the circuit to the load side. A well matched circuit shows complete transfer of power from source to load or vice-versa. In our present scenario, the antenna or the load has an impedance of 50Ω . To obtain the relevant gap impedance, we have to transform that load to about $5\text{ k}\Omega$ in 70 kV-30 A configuration. In the case of NRL gun, this number varies from $10 - 40\text{ k}\Omega$ based on the voltage level achieved. Thus, the impedance needs to increase by two or three orders of magnitude going from the load to the source. This is too large a jump to be realized in a single stage. If on other hand, we could split this transformation into two stages, we can relax/reduce the difficulties. In the fall of 2019, I was a teaching assistant for the Electromagnetic Fields & Waves course at the University of Maryland, College Park. I was teaching smith charts to undergraduate students. As I learned more about this tool, I started to appreciate its impact on designing the impedance matching circuits. This inspired me to design the multi stage power extraction circuit described in detail in the next few sections.

4.2 Two-Stage Power Extraction Circuit

A two stage power extraction circuit has two inductor-capacitor pairs arranged as shown in the in Figure 4.1. This circuit has two advantages over the single stage circuit shown in Figure 1.4. First, it has two stages, which will lead to less stringent demands on the inductor quality factor. Second, the configuration is such that the DC component of the beam current returns to ground through an inductor ($L_{p,2}$),

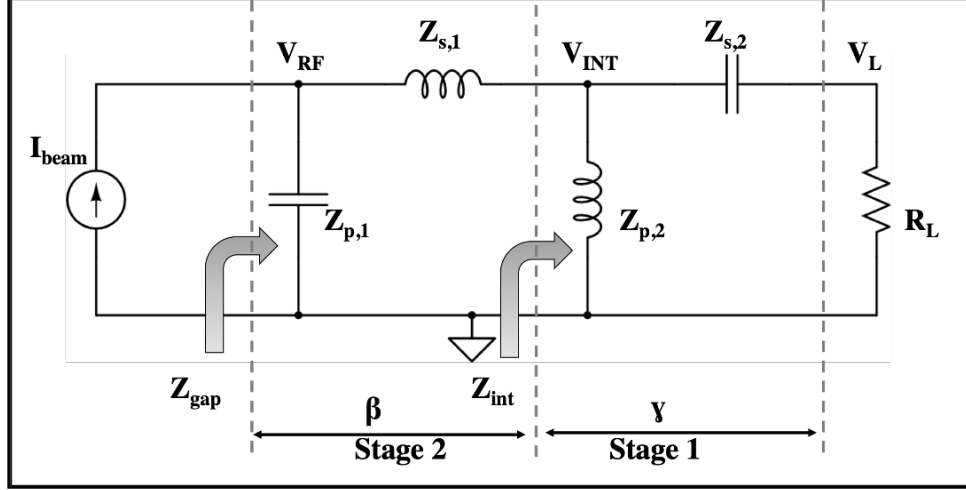


Figure 4.1: A two stage power extraction circuit design

rather than through the load. At resonance the circuit presents a real impedance R_{gap} to the source. The power entering the circuit should be almost entirely delivered to the load resistor,

$$\frac{|V_{RF}|^2}{R_{gap}} = \frac{|V_L|^2}{R_L} \quad (4.1)$$

where the voltages are complex numbers and the relation applies to their magnitudes. Defining the ratio,

$$\alpha = \sqrt{\frac{R_{gap}}{R_L}}, \quad (4.2)$$

we have,

$$\left| \frac{V_{RF}}{V_L} \right| = \alpha \quad (4.3)$$

Let the impedance of the inductors and capacitors be defined as

$$Z_{p,1} = \frac{1}{j\omega C_{p,1}}, \quad (4.4)$$

$$Z_{s,1} = R_{s,1} + j\omega L_{p,1}, \quad (4.5)$$

$$Z_{p,2} = R_{p,2} + j\omega L_{p,2}, \quad (4.6)$$

$$Z_{s,2} = \frac{1}{j\omega C_{s,2}}, \quad (4.7)$$

where the subscripts p,1 and s,1 stand for first parallel and first series elements respectively in the circuit when looking in from the source side.

The assumption that power dissipated $R_{s,1}$ and $R_{p,2}$ is small will put an upper limit on their value. We can safely assume $R_{s,1} \ll X_{s,1}$ and $R_{p,2} \ll X_{p,2}$ and ignore the real part in our calculations for the time being.

Elements $C_{s,2}$ and R_L form a voltage divider. Let us define a new ratio,

$$\gamma = \left| \frac{V_{int}}{V_L} \right| = \left| 1 + \frac{1}{j\omega C_{s,2} R_L} \right| = \sqrt{1 + \frac{1}{(\omega C_{s,2} R_L)^2}} \quad (4.8)$$

$$\therefore \gamma^2 = 1 + \frac{1}{(\omega C_{s,2} R_L)^2} \quad (4.9)$$

.

Alternatively, we can define γ' as,

$$\gamma' = \frac{1}{\omega C_{s,2} R_L} = \sqrt{\gamma^2 - 1} \quad (4.10)$$

.

Since we know the R_{gap} and R_L , the value of α for a given configuration is fixed. If γ was the voltage ratio of the first stage, we can define voltage ratio for the second stage as β as

$$\beta = \left| \frac{V_{RF}}{V_{int}} \right| \quad (4.11)$$

such that,

$$\alpha = \beta\gamma \quad (4.12)$$

Finally, the impedance of the first stage, Z_{int} is given by,

$$Z_{int} = \frac{j\omega L_{p,2}(R_L + \frac{1}{j\omega C_{s,2}})}{R_L + \frac{1}{j\omega C_{s,2}} + j\omega L_{p,2}}. \quad (4.13)$$

Let us analyze the next stage defined by the elements $C_{p,1}$, $L_{s,1}$ and Z_{int} . Elements $L_{s,1}$ and Z_{int} form a voltage divider system and we write

$$\beta = \left| \frac{V_{RF}}{V_{int}} \right| = \left| 1 + \frac{j\omega L_{s,1}}{Z_{int}} \right| \quad (4.14)$$

Let us define variables ,

$$A = \frac{L_{s,1}}{L_{p,2}} \quad (4.15)$$

, and

$$B = \frac{\omega L_{s,1}}{R_L} \quad (4.16)$$

.

Using Eq 4.10 in Eq 4.13 , we can square and rewrite Eq 4.12 as,

$$\alpha^2 = \beta^2\gamma^2 = \left((1 + A - B(\gamma'/\gamma^2))^2 + B^2 \right) \gamma^2 \quad (4.17)$$

We then proceed to solve the quadratic equation, keep the positive root and obtain the relation,

$$\frac{1}{\gamma'} = \frac{1 + A}{B + \sqrt{\alpha^2 - (1 + A)^2}} \quad (4.18)$$

We define B as the *operating point* for the circuit similar to a single stage system.

We can now write the admittance of the circuit Y_{gap} as

$$Y_{gap} = j\omega C_{p,1} + \frac{1}{Z_{int} + j\omega L_{s,1}}. \quad (4.19)$$

4.2.1 Losses

We now proceed to find the losses in the system. The losses for the two stage circuit come from two inductors. For the parallel inductor component, we can write

$$f_{x2} = \frac{P_{p,2}}{P_L} = \frac{\left| \frac{V_{int}}{Z_{p,2}} \right|^2 R_{p,2}}{\left| \frac{V_L}{R_L} \right|^2 R_L} = \left(\left| \frac{V_{int}}{V_L} \right|^2 \left| \frac{R_L}{Z_{p,2}} \right|^2 \right) \left(\frac{R_{p,2}}{R_L} \right) \cong \frac{\gamma^2 R_L^2}{L_{p,2}^2} \left(\frac{R_{p,2}}{R_L} \right) = \frac{\gamma^2 A^2}{B^2} \left(\frac{R_{p,2}}{R_L} \right) \quad (4.20)$$

Similarly, we can derive the equation for the losses in the series inductor as follows:

$$f_{x1} = \frac{P_{p,1}}{P_L} = \frac{\left| \frac{V_{int}}{Z_{int}} \right|^2 R_{s,1}}{\left| \frac{V_L}{R_L} \right|^2 R_L} = \left(\left| \frac{V_{int}}{V_L} \right|^2 \left| \frac{R_L}{Z_{int}} \right|^2 \right) \left(\frac{R_{s,1}}{R_L} \right) \cong \left(\frac{\gamma A}{B} - 1 \right)^2 \left(\frac{R_{s,1}}{R_L} \right) \quad (4.21)$$

We can write the resistances in terms of Quality Factor as ($R_{s,1} = \omega L_{s,1} Q_{s,1}^{-1}$ and $R_{p,2} = \omega L_{p,2} Q_{p,2}^{-1}$) and write the ratio of total dissipated power in the resistances to the load as ,

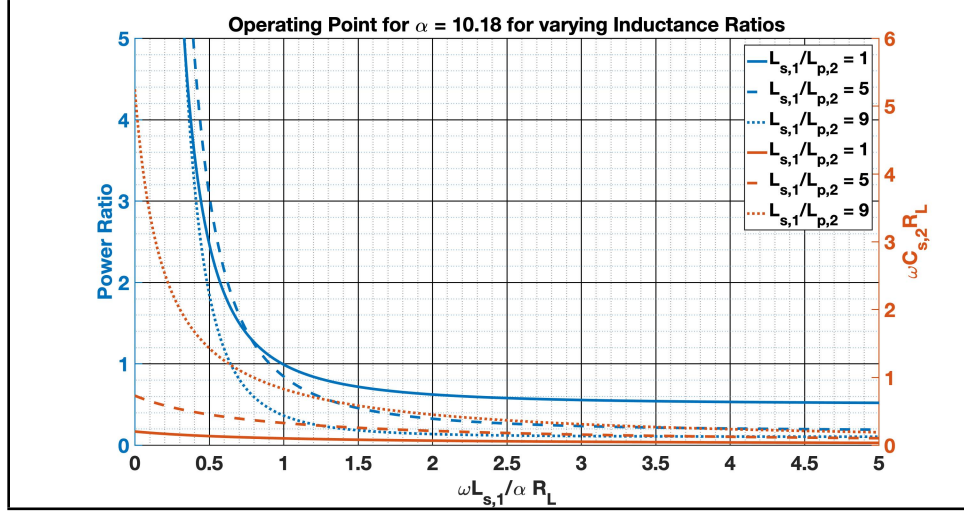


Figure 4.2: Finding the Operating Point with losses minimized.

$$\begin{aligned}
 \therefore \frac{P_{diss}}{P_L} &= f_{x1} + f_{x2} \\
 &= \frac{\gamma^2 A^2}{B^2} \left(\frac{\omega L_{p,2} Q_{p,2}^{-1}}{R_L} \right) + \left(\frac{\gamma A}{B} - 1 \right)^2 \left(\frac{\omega L_{s,1} Q_{s,1}^{-1}}{R_L} \right) \\
 &= \frac{\omega L_{s,1}}{R_L} \left[\frac{\gamma^2 A^2}{AB^2} Q_{p,2}^{-1} + \left(\frac{\gamma A}{B} - 1 \right)^2 Q_{s,1}^{-1} \right]
 \end{aligned} \tag{4.22}$$

Assuming the Qs are equal ($Q_{s,1} = Q_{p,2} = Q$), one can write the 4.22 as,

$$\frac{P_{diss}}{P_L} = \text{Power Ratio} \frac{\omega L_{s,1} Q^{-1}}{R_L} \tag{4.23}$$

where,

$$\text{Power Ratio} = \left[\frac{\gamma^2 A^2}{AB^2} + \left(\frac{\gamma A}{B} - 1 \right)^2 \right] \tag{4.24}$$

We now have equations similar to the single stage power extraction circuit to find the optimal circuit elements. Obviously, there are a few more variables in the equation because of additional elements. Since we already know the value of α

for our application, we can use that as a constant. We can plot γ'^{-1} as a function of B normalized with respect to α for different values of A . We can also plot the power ratio as a function of B simultaneously. We consider three distinct cases for A : (i) $A \ll \alpha$, (ii) $A \cong \alpha/2$ and finally (iii) $A \rightarrow \alpha$ (radical in the Eq 4.2 should be positive at all times, $\Rightarrow \frac{\alpha}{\gamma} - 1 < A < \alpha - 1$). In Figure 4.2, the blue lines on the plot denotes the power ratio as a function of the operating point. The red lines plot variance of $\omega C_{s,2} R_L$ as a function of the operating point. The blue and the red solid line refer to $A \ll \alpha$. Dashed blue and red lines refer to $A \cong \alpha/2$. Finally, the dotted blue and red lines refer to $A \rightarrow \alpha$. For ideal operation, we want the circuit to have a very low power ratio and good tuning range. We choose to keep the value of A close to α . Physically, this means we choose to maintain a high inductance ratio between the two stages. Finally, we pick the $C_{p,1}$ by solving Eqn 4.19 and setting the imaginary part, $B_{gap} = 0$ at resonance. In the next section, we discuss the simulations performed with these design features in mind.

We choose to operate in the region $B = \omega L_{s,1}/(\alpha R_L) = 0.5$ to 1.7, Let us pick the values of R_{gap} , R_L , α and operating frequency f as below:

$$R_{gap} = 5.18 k\Omega, \quad R_L = 50 \Omega, \quad \text{and} \quad \alpha = 10.18 \quad (4.25)$$

and

$$f = 3 MHz \Rightarrow \omega = 2\pi * 3 * 10^6 \text{rads}^{-1} \quad (4.26)$$

Starting with $\frac{\omega L_{s,1}}{\alpha R_L} = 0.5$, we obtain $L_{s,1} = 13.5 \mu H$. We can read the corresponding $\omega C_{s,2} R_L = 1.43$ and $Power Ratio = 1.85$ from the $\frac{L_{s,1}}{L_{p,2}} = 9$ curve in Figure 4.2. These values help us find the required $C_{s,2}$, $L_{p,2}$. Finally, solving the

admittance equation with all the known values and setting the imaginary part equal to zero will provide us the required $C_{p,1}$. These values are summarized in the Table 4.1

$C_{p,1}$	185.6 pF	R_L	50 Ω
$L_{s,1}$	13.5 μH	ω	$2\pi(3 * 10^6)$
$C_{s,2}$	1.5 nF	R_{gap}	5.18 k Ω
$L_{p,2}$	1.5 μH	V_{RF}	70 kV

Table 4.1: Two stage circuit parameters for 99% efficiency at 3 MHz

Using the circuit parameters in Table 4.1 and the power loss equations, we can calculate efficiencies for different winding resistances (and Q). Table 4.2 shows the winding resistances for three different dissipation ratios (f_x).

P_{diss}/P_L	Power Ratio	$R_{s,1}$	$R_{p,2}$	$Q_{s,1 \text{ or } p,2}$
0.01	1.85	270 m Ω	30 m Ω	940
0.05	1.85	1.36 Ω	151 m Ω	187
0.1	1.85	2.7 Ω	300 m Ω	94

Table 4.2: Winding Resistances for different dissipation factors

$C_{p,1}$	16.31 pF	R_L	50 Ω
$L_{s,1}$	13.5 μH	ω	$2\pi(10 * 10^6)$
$C_{s,2}$	169.12 pF	R_{gap}	5.18 k Ω
$L_{p,2}$	1.5 μH	V_{RF}	70 kV

Table 4.3: Two stage circuit parameters for 99% efficiency at 10 MHz

4.2.2 Tunability

Let $B = B_0 = \omega_0 L_{s,1}/(\alpha R_L)$ be the operating point. We choose an operating range to provide for tunability. For the two inductor coils used in the circuit, operating over a range, say from $\omega L_{12}/\alpha R_L = 0.5$ to 1.7, is reasonable. The needed capacitance will vary by a factor of about 2 and the power ratio will be below 2. However, if one attempts to increase the range $\omega L_{12}/\alpha R_L = 0.4$ to 2, at the low frequency end the power ratio doubles and the range of capacitance needed is factor of 4. These are undesirable for high efficiency and practically realizable circuits. By choosing to operate between 0.5 and 1.7, the tuning range for frequency becomes limited. Table 4.3 captures the circuit parameters at 10 MHz. Notice that the inductors are fixed and capacitors are variable.

4.3 Simulations & Results

A PSpice simulation is performed with the above values to validate the the design equations. Figure 4.3 is the PSpice schematic of the two stage power extrac-

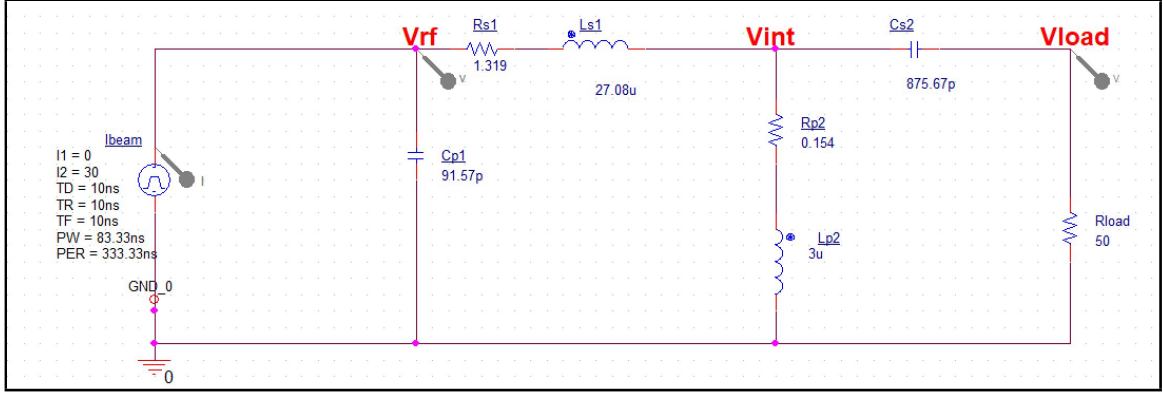


Figure 4.3: PSpice simulation schematic for the two stage power extraction circuit.

tion circuit. The RF gun is mimicked by the beam current source. The rest of the elements are summarized in the table above. We plot the voltages and impedances of the circuit as a function of the frequency. Figure 4.4 shows the gap voltage peak at the resonant frequency of 3 MHz.

The voltage at the load is around 7kV at resonance. The impedance of the circuit is plot as a function of the frequency in Figure 4.5. We see, the resonant gap impedance , R_{gap} is at the desired level of $5.1 k\Omega$.

Using the circuit parameters and the power loss equations, we can calculate efficiencies for different winding resistances. Table 4.2 shows the winding resistances for three different dissipation ratios (f_x). We have assumed the winding resistances have the same ratio as the inductances for equitable distribution.

The efficiency of the circuit is calculated by substituting all the values in Eq 4.22 and we obtain

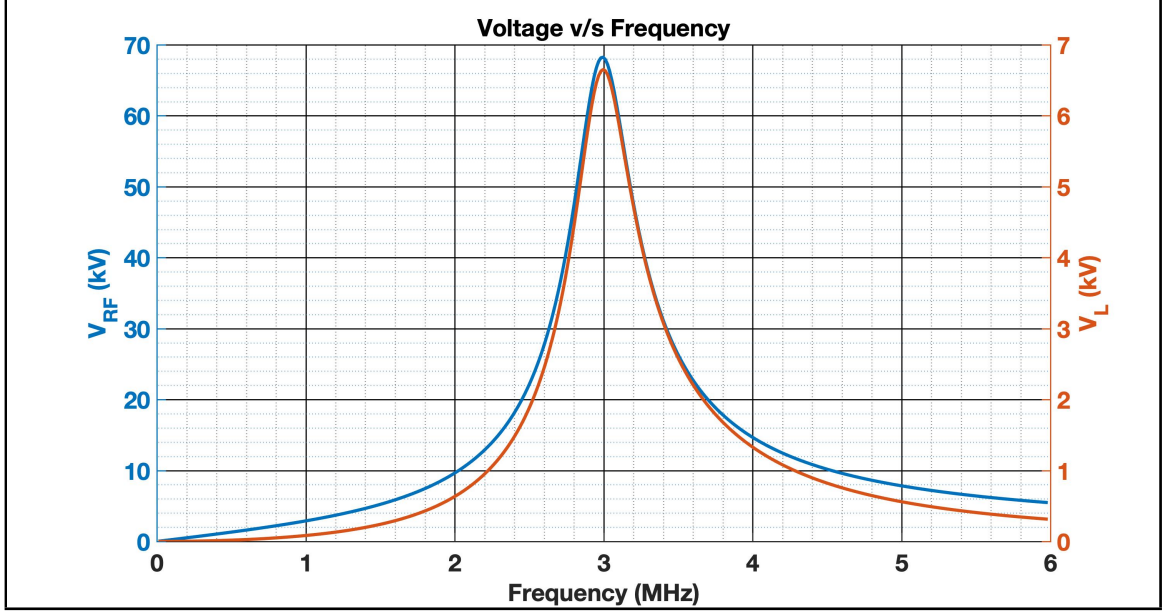


Figure 4.4: V_{RF} (blue) and V_L (red) plots as a function of the frequency in two stage circuit.

$$(f_x) = f_{x1} + f_{x2} = \frac{\gamma^2 A^2}{B^2} \left(\frac{R_{s,1} + R_{p,2}}{R_L} \right) = 1\% \quad (4.27)$$

and therefore,

$$\eta = \frac{1}{f_x + 1} = 99\% \quad (4.28)$$

In conclusion, we developed a two stage power extraction circuit with low Q inductors. By adding a capacitor $C_{s,2}$ in series with load, we essentially blocked the DC component of the beam current entering the load. In theory both designs are valid. However, the two stage power extraction circuit is a practically realizable circuit. We may recall that in Chapter 2 we found that the design necessitated the quality factor to be so high, it made the circuit extremely sensitive to small

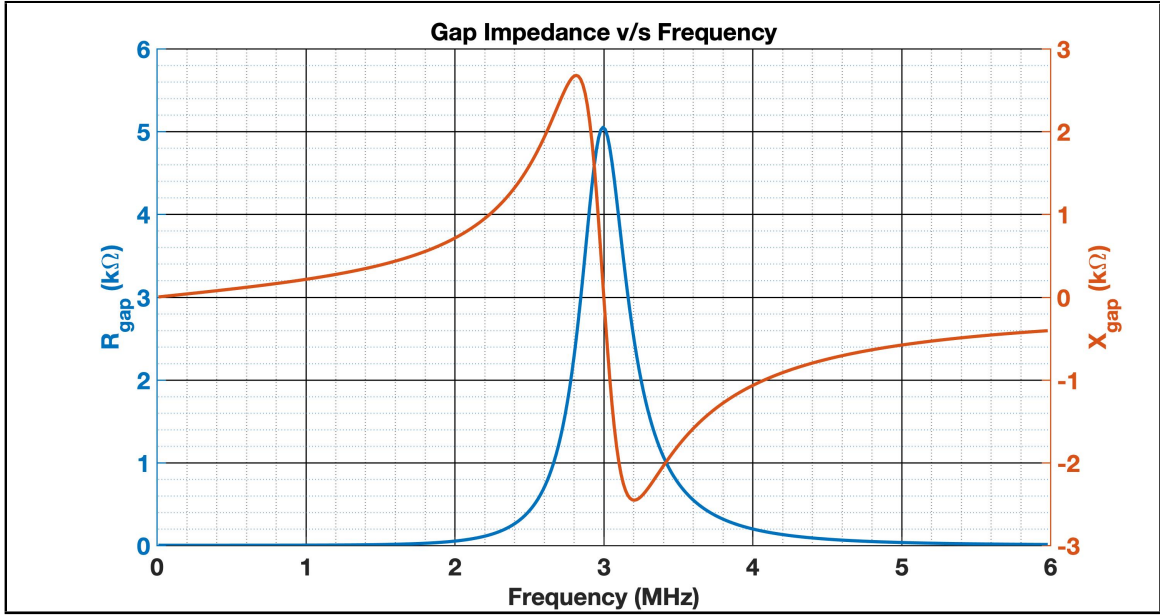


Figure 4.5: R_{gap} (blue) and X_{gap} (red) plots as a function of the frequency in two stage circuit.

changes in their values. Testing the device was an added complication as the error in testing was directly proportional to the quality factor of the device. Hence, we see a relaxation in terms of individual component design as well as the overall circuit. Tunability is no longer an issue because of two stages. We now have sufficient room to explore the entire frequency band from 3 - 10 MHz using a pair of fixed inductors. Thus, we have a proof of principle two stage power extraction extraction circuit that promises high efficiency, good tunability which can be built and tested with physically realizable circuit elements.

Chapter 5: Conclusion

Mobile Ionospheric Heaters will allow for the first time, quantitative exploration of the ionosphere at different geomagnetic latitudes. These mobile structures must be relatively smaller than the existing arrays (small enough to fit on the barge of a ship) and highly efficient at the same time. The size and efficiency of the terrestrial heating units prevent their reuse in mobile structures. These factors motivate the need for developing novel heater units. Our research focused on a new high power, high-efficiency RF source that consists of a gridless tetrode RF tube and a highly efficient power extraction circuit. My research addresses the characterization and optimization of the power extraction circuit.

The goal of this thesis was to design high power, high efficiency tunable constant impedance power extraction circuits for mobile ionospheric heaters. In Chapter 1, we introduced the the idea of ionospheric modification, its importance and the means to achieve it. We described the existing heaters and their advantages and disadvantages in the present context. We briefly introduced all the sub systems in a mobile ionospheric heater unit and described the goal of this research.

Chapter 2 developed a simple pi circuit as a power extraction circuit. We discussed the results from simulations, cold test experiments and an actual experiment

V_{RF}	70 kV	R_{gap}	5.18 k Ω
f	3 MHz	R_L	50 Ω
Single Stage Circuit		Two Stage Circuit	
C_1	259 pF	$C_{p,1}$	185.6 pF
L_{12}	10.8 μH	$L_{s,1}$	13.5 μH
		$L_{p,2}$	1.5 μH
C_2	2.43 nF	$C_{s,2}$	1.5 nF

Table 5.1: Summary of Single Stage and Two Stage Power Extraction Circuits for 70 kV - 30A configuration at 3 MHz

on the NRL gun at multiple frequencies. These experiments established a proof of principle and showed us the limitations of single stage power extraction circuits. Single stage circuits demanded high Q circuit elements for high efficiency. Our research efforts on the transformer was presented at the International Vacuum Electronics Conference-2016 [21]. The single stage circuit simulations were presented at the International Conference of Plasma Science -2017 [20]. Experiments on the NRL gun were published in [18].

Chapter 3 dealt with a novel approach to design high Q inductors at MHz frequency range. We discussed different parasitics (skin effect, proximity effect and self resonance) that plagued the inductor design at higher frequencies and suggested a method to control their influence. We modeled these effects using Maxwell sim-

ulations and tested the predictions. We realized that errors in measurement were very high for high Q inductors and hence couldn't validate our design approach.

Finally, in Chapter 4 we discuss a two stage power extraction circuit that overcomes the shortcomings of the single stage circuits and demanded relatively lower Q inductors. Table 5.1 and 5.2 summarize the power extraction circuit design in single stage and two stage systems for 70 kV - 30A gun configuration at 3 MHz frequency.

Our research finds that the impedance transformation from beam to load (two orders of magnitude) imposes severe restrictions on single-stage design. Additionally, measurements of high Q components aren't very reliable at higher frequencies. We proposed a two-stage power extraction circuit that resolves both of these problems. Simulation results show a circuit design that is expected to yield the desired efficiency. The findings from the research in this thesis would help in the eventual construction and testing of the MW RF heating system that would facilitate a mobile heater for IM research in the future.

$\eta = 99\%$			
R_{12}	$80\text{ m}\Omega$	$R_{s,1}$	$270\text{ m}\Omega$
		$R_{p,2}$	$30\text{ m}\Omega$
Q	2544	Q	939
$\eta = 95\%$			
R_{12}	$400\text{ m}\Omega$	$R_{s,1}$	$1.36\ \Omega$
		$R_{p,2}$	$151\text{ m}\Omega$
Q	508	Q	187
$\eta = 90\%$			
R_{12}	$800\text{ m}\Omega$	$R_{s,1}$	$2.7\ \Omega$
		$R_{p,2}$	$300\text{ m}\Omega$
Q	254	Q	94

Table 5.2: Winding Resistances and inductor Qs essential for design at different efficiencies for 70 kV - 30A configuration at 3 MHz

Bibliography

- [1] Birkeland, Kristian (1908). The Norwegian Aurora Polaris Expedition 1902-1903. New York and Christiania (now Oslo): H. Aschehoug & Co. out-of-print, full text online.
- [2] Rino CL (2011) The theory of scintillation with applications in remote sensing. IEEE Press, Wiley, Inc. Publication.
- [3] Tulegenov, B., Streltsov, A. V., Kendall, E., McCarrick, M. J., & Galkin, I. A. (2019). Artificial aurora produced by HAARP. *Journal of Geophysical Research: Space Physics*, 124, 3255–3265. <https://doi.org/10.1029/2019JA026607>.
- [4] Greer, K. R., Immel, T., and Ridley, A. (2017), On the variation in the ionospheric response to geomagnetic storms with time of onset, *J. Geophys. Res. Space Physics*, 122, 4512–4525, doi:10.1002/2016JA023457.
- [5] Zell, Holly (2015-03-02). "Earth's Upper Atmosphere". NASA. Retrieved 2017-02-20.
- [6] Sturman, A.P. & N. Tapper 1996. *The Weather & Climate of Australia and New Zealand* (Oxford) 476pp.
- [7] Crutcher, H.L. 1969. Temperature & humidity in the troposphere. In *Rex* 1969, 45-84 (3).
- [8] "The Stratosphere - overview". scied.ucar.edu. University Corporation for Atmospheric Research. Retrieved 25 July 2018.
- [9] States, R.J. and C.S. Gardner, 2000: Thermal Structure of the Mesopause Region (80105 km) at 40N Latitude. Part I: Seasonal Variations. *J. Atmos. Sci.*, 57, 6677, [https://doi.org/10.1175/1520-0469\(2000\)057;0066:TSOTMRj2.0.CO;2](https://doi.org/10.1175/1520-0469(2000)057;0066:TSOTMRj2.0.CO;2)
- [10] Windows to the Universe team (2008). *The Thermosphere*. Retrieved , from <http://www.windows2universe.org>.

- [11] VanBlaricum, G. F. Ostrowsky, H. S., Ionospheric Modification: Its Effects on Radar and Satellite Communication Systems.
- [12] K. Rawer. Wave Propagation in the Ionosphere. Kluwer Acad.Publ., Dordrecht 1993
- [13] Gillmor, C. The history of the term ionosphere. Nature 262, 347348 (1976). <https://doi.org/10.1038/262347a0>
- [14] E. V. Appleton, "Wireless studies of the ionosphere," in Journal of the Institution of Electrical Engineers, vol. 71, no. 430, pp. 642-650, October 1932, doi: 10.1049/jiee-1.1932.0144.
- [15] RUSSELL, A. The Kennelly-Heaviside Layer. Nature 116, 609 (1925). <https://doi.org/10.1038/116609c0>
- [16] Powerful electromagnetic waves for active environmental research in geospace, by T. B. Leyser and A. Y. Wong (Reviews of Geophysics, Vol. 47, RG1001, 2009).
- [17] R. Seviour, "Comparative Overview of Inductive Output Tubes", ESS report, June 2012.
- [18] B. L. Beaudoin et al., "Scaled experimental studies on radio frequency source for megawatt-class ionospheric heaters," 2018 IEEE International Vacuum Electronics Conference (IVEC), Monterey, CA, 2018, pp. 21-21, doi: 10.1109/IVEC.2018.8391532.
- [19] Jean Delayen (Thomas Jefferson National Accelerator Facility Old Dominion University) presentation on Cavity Design, First Mexican Particle Accelerator School Guanajuato, 26 Sept-3 Oct 2011.
- [20] A. H. Narayan et al., "Simulations Of Power Extraction Circuits For Mobile Ionospheric Heating*," 2017 IEEE International Conference on Plasma Science (ICOPS), Atlantic City, NJ, 2017, pp. 1-1, doi: 10.1109/PLASMA.2017.8496150.
- [21] A. H. Narayan, B. L. Beaudoin, C. Turner, N. Goyal and T. M. Antonsen, "Constant impedance tunable IOT power extraction circuit," 2016 IEEE International Vacuum Electronics Conference (IVEC), Monterey, CA, 2016, pp. 1-2, doi: 10.1109/IVEC.2016.7561771.
- [22] Horace Lamb and James Whitbread Lee Glaisher 1997XIII. On electrical motions in a spherical conductor Phil. Trans. R. Soc. 174519549.

- [23] O. Heaviside to H. Hertz (13 July 1889), in J. G. O Hara, W. Pricha, Hertz and the Maxwellians: A Study and Documentation of the Discovery of Electromagnetic Wave Radiation, 18731894, Peter Peregrinus, London (1987), p. 67.
- [24] Terman, F.E. Radio Engineers' Handbook, McGraw-Hill 1943 details electromagnetic proximity and skin effects
- [25] P. L. Dowell, "Effects of eddy currents in transformer windings," in Proceedings of the Institution of Electrical Engineers, vol. 113, no. 8, pp. 1387-1394, August 1966, doi: 10.1049/piee.1966.0236.
- [26] Kazimierczuk, Marian K. High-frequency magnetic components. John Wiley & Sons, 2009.
- [27] Beaudoin, Brian L., et al. "Experimental studies on radio frequency sources for ionospheric heaters." Physics of Plasmas 25.10 (2018): 103116.
- [28] Sprangle, Phillip, et al. "High average current electron guns for high-power free electron lasers." Physical Review Special Topics-Accelerators and Beams 14.2 (2011): 020702.
- [29] Beaudoin, Brian L., et al. "Experimental Measurements of Power Extraction Circuits For Mobile Ionospheric Heating." 2017 IEEE International Conference on Plasma Science (ICOPS). IEEE, 2017.
- [30] Z. Pantic and S. Lukic, "Computationally-Efficient, Generalized Expressions for the Proximity-Effect in Multi-Layer, Multi-Turn Tubular Coils for Wireless Power Transfer Systems," in IEEE Transactions on Magnetics, vol. 49, no. 11, pp. 5404-5416, Nov. 2013, doi: 10.1109/TMAG.2013.2264486.
- [31] <https://en.wikipedia.org/wiki/Solenoid#/media/File:Solenoid-1.png>
- [32] F. N. Javidi and M. Nymand, "A New Method for Measuring Winding AC Resistance of High-Efficiency Power Inductors," in IEEE Transactions on Power Electronics, vol. 33, no. 12, pp. 10736-10747, Dec. 2018, doi: 10.1109/TPEL.2018.2805867.
- [33] Foo, Benedict X., Aaron LF Stein, and Charles R. Sullivan. "A step-by-step guide to extracting winding resistance from an impedance measurement." 2017 IEEE Applied Power Electronics Conference and Exposition (APEC). IEEE, 2017.

- [34] Sullivan, Charles R. "High-frequency magnetics design: Overview and winding loss." Dartmouth Magnetics and Power Electronics Research Group. Thayer School of Engineering at Dartmouth (2016).